Nucleation and growth of gas bubbles in AlSi8Mg4 foam investigated by X-ray tomoscopy

Paul Hans Kamm[a,b,*], Tillmann Robert Neu[a,b], Francisco García-Moreno[a,b], John Banhart[a,b]

[a] *Institute of Applied Materials, Helmholtz-Zentrum Berlin für Materialien und Energie, Hahn-Meitner-Platz 1, 14109 Berlin, Germany*
[b] *Institute of Materials Science and Technology, Technische Universität Berlin, Hardenbergstr. 36, 10623 Berlin, Germany*

* Corresponding author. E-mail address: paul.kamm@helmholtz-berlin.de; Phone: +49 30 314 29228 (P.H. Kamm).

Abstract

Initiation and growth of metal foam is a complex and dynamical process, which is intrinsically three-dimensional and time-dependent. Tomoscopy –or time-resolved tomography– allows us to follow the nucleation and growth of gas bubbles in AlSi8Mg4 alloy in real time during foaming. The location, size and shape of individual bubbles was determined in steps of 1 s with spatial resolutions of a few µm. Moreover, the constituents responsible for gas evolution, namely Al-Mg phases and TiH_2 particles, were identified in the series of 3D images. Automated quantitative image analysis of bubbles and gas-generated phases including their spatial correlations allowed us to break down the foaming process into two distinct steps, a first homogenous one driven by absorbed gases and first melting microstructural components and a second attributed to the melting of the alloy and subsequent foam growth driven by hydrogen released from TiH_2 particles. The results of the study indicate that standard AlSi8Mg4 foam can be improved by tailoring the properties of the Al-Mg constituent powder.

Keywords: Metal foam, Nucleation and growth, Time-resolved synchrotron tomography, Diffraction, Tomoscopy

1. Introduction

Aluminium foams, a nature-inspired cellular material consisting of a gas phase dispersed in a solid metal matrix, have been the subject of research for almost 100 years due to their unique properties [1]. The objective is their commercial adoption in areas such as lightweight construction, where the emphasis is on weight-related, desirable mechanical properties, or functional applications, which for example aim at the thermal conductivity or the large surface area of the material. Despite intensive research, some mechanisms such as gas nucleation, film stability, drainage and coarsening are not fully understood. The commercial breakthrough has also not yet been achieved due to the high manufacturing costs and the need to optimise the reproducibility of structure and properties, which makes metallic foams a niche product for special applications [2]. There are various manufacturing methods for closed-cell metal foams. In addition to the direct foaming processes, in which gas bubbles or gas-generating blowing agents are introduced into a stabilized melt and then immediately foamed, the indirect route has also become established, in which a foamable precursor material is first produced and then foamed in a second step [3].

As an example, **Fig. 1** presents two tomograms of foams produced indirectly through powder metallurgy. Pure Al (**Fig. 1c**) and the alloy AlSi8Mg4 (**Fig. 1a**) foamed from precursors of equal dimensions in a limited crucible [4] exhibit a similar porosity of ~70 %. The average pore diameter of ~2 mm for AlSi8Mg4 is not only half as large as that of pure Al, but also has a narrower distribution and thus greater homogeneity (see their volume-weighted pore size distributions in **Fig. 1b**), which is very important for predictable mechanical properties [5,6]. It is also known that lower bubble sphericity, as for Al, contributes to a reduction in effective conductivity and elastic modulus [7]. The AlSi8Mg4 foam has a high internal structural stability [8], which can be seen also from the fact that pure Al undergoes higher shrinkage after filling the mould and subsequent cooling. This is also reflected in the number of pores determined in the solid foam, which is with 10000 pores for AlSi8Mg4 about ten times higher than for pure Al. The reasons for this difference in number, size and shape of pores are the mechanism of nucleation of the gas bubbles in the initial and the stability of the cell walls in the later stage.

Models of nucleation can be divided into homogeneous and heterogeneous. The homogeneous nucleation of gas bubbles in a supersaturated aluminium melt requires hydrogen partial pressures that are many times higher than can be achieved by adding the usual amounts of blowing agent [9]. It can therefore be excluded for the system under consideration. The heterogeneous nucleation of the gas bubbles can occur in different components of the powder metallurgically produced system. In particular, the blowing agent particles, oxides and weak points in the matrix (e.g. low-melting components) were identified as the starting points of bubble formation [10,11].

One reason for the superior foam structure and foamability of the alloy AlSi8Mg4 is the good powder compactability with relative densities of more than 98 % and a metallic bonding between the powder particles leading to gas-tight precursors [12]. This prevents cracks from forming during the foaming step, along which the gas produced could escape and thus not contribute to foam volume expansion [13]. A further advantage of the alloy is the large proportion of melt that is produced in a small temperature interval [14]. An optimum range of 40-60 % melt just above the solidus temperature, with the presence of sufficient solid particles to stabilize the melt, leads to good expansion and foam structure [15].

Modern synchrotron radiation sources with their very intense X-rays combined with the latest developments of detectors, provide a three-dimensional, time-resolved insight into the evolution of foaming in the sub-second range over a period of minutes with high spatial resolution [16,17]. The alloy dependence of gas nucleation was investigated ex-situ by tomography on frozen samples interrupted during foaming [11], but only recently has this been possible in-situ [18]. An additional, simultaneous use of diffraction enables experiments that provide a direct comparison of macrostructure evolution with chemical or phase transformations during foaming [19].

In this work, the important step of gas nucleation and bubble growth in powder metallurgically produced aluminium foams is investigated since it has a significant influence on the later foam structure. To achieve this, the method of tomoscopy was used, as well as with simultaneous diffraction, to visualise and quantitatively analyse the phenomena and phases occurring in aluminium foams.

2. Experimental

2.1 Sample Preparation

Foamable precursors were made from elemental and pre-alloyed metal powders as stated in **Table 1**. The powder size distributions were measured on dry powders by laser diffraction using the LS 13 320 particle size analyser (Beckman Coulter, USA). The powders were weighted according to the composition of the alloy AlSi8Mg4 (in wt%) with an addition of 0.25 wt% of the heat-treated blowing agent TiH_2 and mixed in a tumbling mixer for 30 min. Their thermal pre-treatment lasting 3 h at 480 °C in air atmosphere allowed for an oxide shell to grow around the blowing agent particles acting as a diffusion barrier, delaying the hydrogen release dynamics in the foaming process and shifting it to higher temperatures [20–22]. The powder blends were first uniaxially cold and then hot compacted following a well-established recipe at a temperature of 400 °C with a pressure of 300 MPa for 15 min reaching a nearly dense state [12]. The resulting tablets with a mass of ~30 g were milled into pieces of a dimension of 4 mm × 4 mm × 2 mm.

2.2 Precursor Analyses

Light microscopic images were taken with an Axioplan 2 microscope (Carl Zeiss, Germany). Scanning electron microscopic (SEM) investigations with energy dispersive X-ray spectroscopy (EDX) for local determination of the elemental composition in the microstructures were performed on a Gemini 1530 (LEO Electron Microscopy, UK).

2.3 Synchrotron X-Ray Tomoscopy

Tomoscopy, which is time-resolved 3D tomography applied to a system undergoing dynamic changes and monitoring various stages of its evolution in a continuous manner, was carried out at the *TOmographic Microscopy and Coherent rAdiology experimenTs* beamline (TOMCAT) of the Paul Scherrer Institute's Swiss Light Source, Villigen, Switzerland and at the *Energy Dispersive DIffraction* beamline (EDDI) at the BESSY II synchrotron facility of the Helmholtz-Zentrum Berlin, Germany. The polychromatic radiation generated by a superconducting 2.9 T bending magnet (TOMCAT) or 7 T multipole wiggler (EDDI) was filtered using either 325 µm of Si or 1 mm of Al, respectively, to lower the heat load on the setup induced by low energy X-rays. At both beamlines, a high-speed CMOS camera DIMAX HS4 (PCO, Germany) with a sensor size of 20016 × 2016 pixel with a pitch of 11 µm in conjunction with a 150 µm (TOMCAT) or 200 µm (EDDI) thick LuAG:Ce scintillator (CRYTUR, Czech Republic), a mirror to displace the camera from the direct beam and an optical lens with variable magnification (**Fig. 2**) leading to a pixel size between 2.5 μm and 5 μm in the resulting images was used to acquire radiographic projections with frame rates between 200 fps (EDDI) and 5000 fps (TOMCAT). The recorded images covered a cropped field of view (FoV) of either 2 mm × 0.75 mm (TOMCAT) or 3.8 mm × 2 mm at EDDI, respectively. In both cases, 500 projections were taken over an angle of 180° to reconstruct a 3D volume using either the filtered back projection or the *gridrec* algorithm [23,24]. At rotation speeds of $72°\text{s}^{-1}$ and $1800°\text{s}^{-1}$ this resulted in a repetition rate of 0.4 Hz (EDDI) or 1 Hz (TOMCAT). In the latter, only every tenth tomogram was acquired in a sequential mode in order to get sharper temporal delimited tomograms for an extended period of time. Another series of measurements was performed with the GigaFRoST camera system, which is based on the same image sensor but allows for a longer recording time while maintaining the same high temporal resolution [25].

Foaming of the samples was either done inside a boron nitride (BN) crucible with an inner diameter of 8 mm, which was heated by a 2 × 150 W (980 nm) infra-red (IR) laser system (Apollo Instruments, USA / TOMCAT) [18,26] or using a self-made 150 W IR lamp furnace (EDDI) [19]. A temperature calibration was performed by a second thermocouple touching the sample during a reference measurement at both beamlines. The temperature itself was measured either by a pyrometer (Optris, Germany) pointing at the crucible (TOMCAT) or by a thermocouple contacting the sample from below through the rotation stage (EDDI).

To perform an intensity correction for the diffraction measurement, the sample density was determined throughout the experiment from the radiographic projections using the Beer-Lambert law $\rho_\text{S}^* = \log\left(I_\text{bkg}^\text{img}(t_0)/I_\text{S}^\text{img}(t)\right)$, with the mean grey value I_bkg^img of a region within the first projections without sample (incident light) and I_S^img the mean grey value in a region that is occupied by the sample over the entire experiment (transmitted light). The extinction of the sample ρ_S^* was normalised to the measured density of the unfoamed precursor (2.54 g cm^{-3}) assuming a constant attenuation coefficient and sample thickness in beam direction.

2.4 Data Analysis

Data analysis was performed in Fiji [27] and MATLAB (MathWorks, USA) using self-developed scripts. The reconstructed 3D volumes were denoised through a median filter and in some cases additionally filtered bilaterally for better subsequent segmentation of low-contrast regions. The binarised volumes in the form of matrix material, highly absorbing blowing agent particles and bubbles or initially present, low-absorbing AlMg particles were further morphologically filtered to remove e.g. noise voxels. In later stages, at high porosities, a watershed transformation was applied for the correct separation of segmented bubbles, as thin cell walls between pores are often not correctly determined due to limited resolution and contrast. 3D visualisation was either done in Avizo (Thermo Fisher, USA) or Dragonfly (ORS, Canada). The porosity was determined from the ratio of the bubble volume to the observation volume, the bubble number density from the volume normalised, separated bubbles. An Euclidean distance transformation was performed on the separated AlMg particles and masked with the separated bubble voxels for each time point in the first pore formation phase. From the values on which the centres of gravity of the bubbles lie, the distance distribution of these bubbles from the edge of the AlMg particles was identified. For each bubble, an equivalent bubble diameter describing the diameter of a sphere of the same volume was evaluated and a principal component analysis performed. This analysis determines an orthogonal base for all voxels belonging to a bubble, the first axis pointing in the direction of the greatest variance of the voxel set

[28]. The eigenvalues of the covariance matrix of this voxel set can be used to calculate the variances in the three coordinate directions, similar to a three-dimensional Gauss distribution. Conclusions about the shape (round, elongated or flat) or the orientation of the individual bubbles can be derived from the ratios and directions of the three spatial extents. The sphericity Ψ can be described as the ratio between the surface of a sphere and the considered object of the same volume [29]. However, this value depends very much on the underlying surface determination algorithm and is not well applicable to gridded data sets of a few voxels. In this work, therefore, the sphericity Ψ of the maximum projection area, determined from the ratio of the projection area of a sphere and the largest projection area of the considered ellipsoid of the same volume, was used [30]. $\Psi = \pi \cdot \sqrt[3]{L \cdot I \cdot S^2} / (\pi \cdot L \cdot I) = \sqrt[3]{S^2/(L \cdot I)}$, with the length of the large, intermediate, and short axis L, I and S, respectively.

2.5 Energy Dispersive Diffraction

The EDDI beamline (Bessy II, Berlin, Germany) offers the unique possibility of acquiring the intensity of energies of the polychromatic beam diffracted by the gauge volume of the sample in addition to imaging. This volume is limited by a secondary slit opening of, in this case, 10 µm, under a fixed angle of 2θ = 6°. The signal, guided through an opening in the imaging head, is recorded with a multi-channel germanium detector (Canberra, France), while capturing the images for the tomoscopic measurements by redirecting the path of visible light through a scintillator-mirror combination shown in the detail magnification of **Fig. 2**. Each measurement, lasting 2.5 s, provides a full spectrum in the range of the energy of the incoming white beam from the 7T wiggler (8–150 keV) [31,32]. The recorded spectra were corrected for dead time (the time in which the detector is saturated), i.e. their absolute counting time was normalised for comparability. The normalised corrected diffracted intensities $I_{\mathrm{corr}}^{\mathrm{diff}}$ correspond according to the following formula to $I_{\mathrm{corr}}^{\mathrm{diff}}(E,t) = \left(I_{\mathrm{meas}}^{\mathrm{diff}}(E,t) - I_{\mathrm{bkg}}^{\mathrm{diff}}(E)\right)/\left(\rho_{\mathrm{S}}(t) \cdot W(E) \cdot A(E,t)\right)$, with the normalised measured diffracted intensities $I_{\mathrm{meas}}^{\mathrm{diff}}$, the normalised background intensities $I_{\mathrm{bkg}}^{\mathrm{diff}}$, the sample density $\rho_{\mathrm{S}}(t)$ determined from the projection images, the correction factor for the filtered wiggler spectrum $W(E)$ and the absorption correction $A(E,t) = \exp(-\mu_{\mathrm{Al}}^{*}(E) \cdot \rho_{\mathrm{S}}(t) \cdot x)$. The attenuation of the X-ray radiation upon passing the sample depends not only on the sample density but also on its energy through photon interaction expressed by the mass attenuation coefficient μ^{*} (mainly atomic photoeffect in the considered energy range). These corrections are important for experiments in which the sample undergoes a large change in density, as during foaming. A problem here is the inhomogeneous material distribution in a foam, which can lead to deviations in the intensities due to the small scattering volume. The rotation of the sample, which is carried out anyway by the tomographic acquisition, is advantageous here, as it allows integration over a larger sample volume. The peak energies and areas of the diffraction pattern were obtained using an iterative nonlinear least-squares solver to fit the diffracted intensities starting from 48 input values (amplitude, mean and standard deviation of 16 Gaussians) and lower and upper boundaries chosen manually from visual assessment of several diffraction patterns throughout the experiment. The description by 15 Gaussian functions for the peaks and one for the background was chosen because it is both the easiest to automate and provides the best match with the data. Random tests on the strongest Al (111) peak showed only a small difference in fit quality between a description by a pure Gaussian function and a Pseudo-Voigt function in the fourth decimal place of R^2, showing a ratio between Gaussian and Lorentzian near one. This is influenced by several sample and instrument related factors (e.g. crystallite size, micro-stresses, sample orientation and geometry, beam characteristics, orifice apertures, etc.). An absolute determination of the individual influencing factors is associated with enormous effort and is not necessarily required in the context of a qualitative evaluation of the peak area ratios. Further corrections, such as for the structure factor of the phases involved, are also required for a complete quantitative phase determination. An internal calibration standard mixed with the precursor in known proportion could also be utilised. However, it is not guaranteed that this standard can be used over the entire foaming process, so only the comparison of the peak areas associated with the phases is therefore carried out. The interplanar spacings d_{hkl} and thus possible reflections of the existing phases were determined using the measured peak energies E_{hkl} via Bragg's law for the energy-dispersive case $E_{hkl} = h \cdot c/(2 \cdot d_{hkl} \cdot \sin\theta)$, with the Planck constant h, speed of light c, fixed angle θ = 3°, and crystal structure data obtained from the literature [33–39]. A second, internal temperature calibration was performed using the temperature-dependent, lattice parameter of silicon [40]. This proved to be particularly helpful in those areas where the sample undergoes non-uniform temperature changes due to melting and solidification.

3. Results

3.1 Gas Nucleation Stages

Tomoscopic measurements of the pore nucleation stage of the alloy AlSi8Mg4 show an early stage (porosity below 25 %) of the foaming sample (**Fig. 3)**. In the 2-mm wide and 0.75-mm high reconstructed vertical slices in the upper part, the Al-rich matrix is grey, the bubbles black and the blowing agent TiH_2 white (marked with arrows) due to high X-ray absorption of titanium compared to the other components. Darker areas (with weaker X-ray absorption than the matrix) are visible and have been outlined in blue for a better identification and represent the former AlMg50 powder particles. The 3D-representation of the separated bubbles (displayed by changing colours) is shown thereunder.

The graph in **Fig. 3** shows the measured bubble density in blue, where each point can be assigned to a tomogram, the porosity in the observed volume (red) and the temperature measurement (grey dashed). The initial temperature overshoot is an artefact caused by the measurement script at that time, which stops the rotary table at the transition from observation to recording mode to synchronize the acquired images with the rotation angle. The bubble nucleation stage of the alloy AlSi8Mg4 shows a behaviour different from that of pure aluminium (see **Fig. A.1**). Remarkable is the two-stage pore development, which is not observed for pure Al. In the first stage, around 480 °C, round bubbles form. They grow locally and join together, resulting in a slight decrease in bubble number density from the maximum of 790 mm^{-3} to 740 mm^{-3}. This occurs preferentially in the areas marked in blue, i.e. in the former AlMg50 particles as shown in the left pictures. The porosity at this stage is low, amounting to less than 2 %. The second increase of the bubble number density at 560 °C leads to more than 2000 mm^{-3} and is associated with a strong increase in porosity to about 20 % shortly after reaching the bubble density maximum. The pores join to form larger ones or they move out of the field of view due to the corresponding foam expansion, as shown in the pictures on the right, leading to a decrease of the density of bubbles below 1600 mm^{-3} although the porosity continues increasing as most bubbles inflate in the course of further gas release.

Fig. 4a shows the sphericity distribution of bubbles normalised by their number for AlSi8Mg4 and its change during foaming of the sample shown in **Fig. 3** over the temperature range between 480 °C and 620 °C. The average bubble sphericity, indicated by the orange line, is highest at the beginning of the bubble formation at 480 °C, linked to the appearance of small and almost spherical bubbles with Ψ = 0.76±0.06. This high degree of sphericity is nearly maintained up to 540 °C, with a fraction of bubbles starting to show lower sphericity already from 500 °C, resulting in a broadened distribution (0.69±0.19 at 540 °C). After a jump to an average of lower values of 0.49±0.16 at 560 °C when the second bubble formation phase begins, the sphericity distribution starts to steadily shift back towards higher sphericity values until it reaches an average of 0.77±0.11 at 620 °C with a more uniform distribution width.

The volume-weighted bubble diameter distributions at the transition to the second bubble formation stage between 550 °C and 560 °C, shown in **Fig. 4b** and being described by a normal distribution up to 556 °C, reveal a gradual increase of average bubble size from 36±11 μm at 550 °C to 50±17 μm at 556 °C. The distribution shifts abruptly to higher values at 558 °C while it cannot be described by a Gaussian anymore (corrected R^2 drops from ~0.95 to <0.5), due to individual bubbles which begin to grow strongly and merge with others as can be observed in the supplementary **Video 1**.

3.2 Influence of Microstructure

To investigate the first bubble formation stage in more detail, a local correlation analysis was performed involving the bubbles, the former AlMg50 and the TiH_2 particles on the data set of the sample AlSi8Mg4 with 0.25 wt% TiH_2 already shown in the previous figures. The spatial correlation between the AlMg50 particles and the bubbles was realized by extracting the areas with the lower grey values (AlMg50 particles) from the first tomogram of the series, which are shown in the 3D renderings in **Fig. 5** (grey objects, top and bottom). The correlation between AlMg50 areas (grey) and bubbles (red) is readily visible in the 3D image in the upper right corner, which shows the sample after 30 s of foaming. A single AlMg50 grain is shown at the bottom. Between 20 s and 25 s experimental time, first coalescence events in the outer region of the particle are observed, marked by red circles. The graph of **Fig. 5** shows the bubble number density curve of the first bubble formation stage (black), which is known from **Fig. 3**, and the fraction of bubbles formed in the former AlMg50 particles in red. Initially, all bubbles are in the above-mentioned areas. After about 7 s, 94 % of the 60 bubbles per mm^3 are still within these areas and after 15 s (530 mm^{-3}) they still account for 84 %. This value barely changes until it falls off at about 26 s. The blue background graph shows the number-weighted distribution of the distances between the centres of gravity of the bubbles formed in large AlMg50 particles and their nearest surrounding particle surfaces. The size of the particles under consideration (equivalent diameter of more than 150 µm) was chosen in such a way that it can be ensured that within the often flat particles (the average ratio between their smallest and intermediate axis is ~0.45±0.21) there is still a second AlMg phase, which will be discussed further in the following paragraphs. The bubbles that form accumulate strongly in the range between 10 µm and 20 µm from the edge within the particle and the distribution only flattens slightly to higher values.

The results of the simultaneous tomoscopy and diffraction experiment of an AlSi8Mg4 sample with 0.5 wt% TiH_2 performed at the EDDI beamline are shown in **Fig. 6**. The volume considered in this experiment was 2 mm × 2 mm × 1.5 mm and the acquisition rate 0.4 Hz (for both tomoscopy and diffraction). The lower part shows the intensity development (logarithmic scale) of the photons diffracted by the sample over the duration of the experiment (bottom axis) or the calibrated temperature (top axis) of the sample. The phases Si, Al, TiH_2, Mg_2Si and Al_3Mg_2 (β) assigned to the peaks are labelled with the corresponding reflection indices. The strongest Al-induced diffraction patterns at 50 keV and 58 keV are shifted in the observed section by about 300 eV to lower energies and remain there until major melting at 610 °C during heating and reappear during cooling again at the same temperature with an energy shift in the further course in the opposite direction. The Si reflections at 38 keV and 62 keV are shifted much less by about 50 eV until they disappear at 580 °C and reappear on cooling at about 540 °C. Initially, Mg_2Si shows weak reflections at 32 keV and 52 keV, which become more pronounced with increasing temperature, disappear at 580 °C with the melting of the sample and reappear during cooling at 540 °C. The fluctuation in the intensity of the Mg_2Si peaks during the cooling stage can be attributed to the FoV. It correlates with the speed of the rotation stage, indicating a peripheral scattering centre, which periodically moves out of and back into the incident beam. A weak TiH_2 (111) peak at 46 keV can be detected over the entire period. A complete solution in the melt is therefore not observed. From about 100 s/430 °C the reflections associated with Al_3Mg_2 (or Al_8Mg_5) disappear at 47 keV, 48 keV and 53 keV and the background intensities with a simultaneous broadening of the distribution, indicating (amorphous) melt formation. These peaks no longer occur after solidification of the sample. The third reflection of this phase (1133) seems to change into the Al (111) reflection when heated. Even below the Al (200) reflection, a local increase in intensity can be seen after Al_3Mg_2 has disappeared. This reflection approaches the Al (111) reflection with increasing temperature. The reflection occurring at about 40 keV is an escape peak due to the Al (111) reflection and the excitation energy of the Ge-K electrons (Ge-K_α: 9.9 keV) of the detector material.

The top part of **Fig. 6** shows vertical slices of the foam at four different times as captured by simultaneous tomoscopy and below them the bubble number density (each circle represents a tomogram), the porosity (dashed line) and the phase fractions (solid lines) determined from the area of the diffraction peaks is given as a function of temperature. A nearly constant heating rate of ~2.8 K s^{-1} and cooling rate of ~4.5 K s^{-1} was employed. The cross-sectional images show the components of the foamable precursor already known from **Fig. 3**, consisting of the white TiH_2 particles, the dark grey AlMg50 master alloy particles, black bubbles, and the Al matrix. In the first picture at 99 s experimental time, bubbles can already be seen at the upper edge, which, due to their early formation and proximity to the surface of the sample, indicate a melt ejection on the surface which is characteristic for this alloy (**Fig. A.3**). These ejections are not yet present in the very first tomogram at 96 s (not shown). This moment of the first bubble formation overlaps with the disappearance of the peaks assigned to the β phase in the energy spectrum. Again, the bubbles form preferentially in the low-melting regions of the former AlMg50 powder particles, as seen in the second image at the end of the first bubble formation stage (139 s). During foaming abrupt structural rearrangements occur, leading to motion artefacts due to the insufficient time resolution for these events (third image at 159 s). The stable liquid foam, shortly before the onset of solidification, can be seen in the last image (179 s).

The bubble number density qualitatively follows the trend already known from **Fig. 3**, but at slightly higher values of 1400 mm^{-3} at the first maximum (at 510 °C) and 2800 mm^{-3} at the global maximum of the second bubble formation stage (at 560 °C). As already seen for the experiment in **Fig. 3**, the porosity increases only slightly to about 2 % in the first bubble formation stage, then more strongly until the curve flattens, runs through a maximum at 76 % and stabilizes at 74 % towards the end. A further local maximum is observed shortly before solidification begins at 610 °C/180 s. The determination of phase fraction was performed on the diffraction patterns of Al, Si, Al_3Mg_2 Mg_2Si and TiH_2. An initially slight (15 % to 150 s/570 °C) and then a strong decrease of the solid phase fraction (sum of the individual, determined phases) can be seen, which has already completely disappeared after 165 s at 600 °C. The calculated proportion of Al decreases with the same course starting at 75 % and accounts for most of the solid phase until complete melting. The Si content decreases slowly from about 12 % to 9 % at 145 s/550 °C. The slightly higher value compared to the weighed 8 % is possibly due to the fact that the atomic scattering factors of the individual phases are not taken into account. For example, this factor is higher for Si than for Al. During the same period, the Mg_2Si content increases from 2 % to 4 % until both disappear completely at 155 s/580 °C. The proportion of Al_3Mg_2 decreases from about 100 s/430 °C within 20 s from 10 % to 6 % and is later only represented by the peaks close to the Al peaks, both of which disappear with the overall melting. Only the fraction of undissolved TiH_2 is visible with about 1 % (and a maximum fraction of 3 % during melting and solidification) over the whole experiment. Shortly after entering the cooling stage at 175 s, a two-stage solidification takes place at about 600 °C (8 % solidified, mostly Al) and 550 °C, at the end of which the proportion of Al increases to 75 %, Si to 12 % and Mg_2Si to 6 % of the total 93 % determined solid phase. The difference in the total amount of solid fraction at the end is due to a higher background noise because of the lower foam density and thus smaller signal to noise ratio in scattered intensities.

Fig. 7a shows a scanning electron microscope image of a former AlMg50 powder particle embedded in the AlSi8Mg4 alloy precursor containing 0.25 wt% TiH_2. An EDX) line scan along the blue line and in the direction of the white arrow is shown in **Fig. 7b**. The former AlMg50 particle is divided into two regions after compaction. In the centre it consists of the γ-$Al_{12}Mg_{17}$ phase, and the approximately 25 µm wide region surrounding the core consists of β-Al_3Mg_2. At the interface to the Si particle (**Fig. 7a**, right, dark grey) the Mg_2Si phase has formed (black). The neighbouring Al particle shows a Mg content decreasing from about 18 at% (~85/380 counts) with increasing distance as seen on the left in **Fig. 7b**. Separated by the Si particle, however, it has dissolved little to no Mg.

The change in the microstructure of the precursor after compression after a one-hour sintering process at 400 °C is shown in **Fig. 8**. An increase in thickness of the surface layer of the AlMg50 particles from 25 µm to 70 µm, as well as a strong increase in the Mg_2Si content (also visible by changes in the Si particles) and in porosity can be observed in the light microscopic images on the right side from the non-sintered (**Fig. 8a**) to the sintered (**Fig. 8b**) sample. In the tomographic images (left) it is even possible to distinguish the inner phase boundary of the large particles (as indicated for two particles). Due to its small difference in absorption to AlMg50 (the difference in attenuation length between Al_3Mg_2 and Mg_2Si of ~7 % in the range of 10 keV to 30 keV is about as large as between Si and Al with ~11 % whereas it is 23 % between Al and Al_3Mg_2 [41]) and the small size of the individual regions, Mg_2Si cannot be directly determined and can only be guessed in some places (for example at the upper edge of the large, marked AlMg particles, where a slightly brighter Si particle marked by white arrows can be seen). The pores in the sintered precursor can be found preferably at these places, but also elsewhere along the edge of the large AlMg particles and distributed in the Al matrix. The porosity determined from the tomograms corresponds to a fifty-fold increase to 0.25 % after sintering, although the values determined by this method are lower than in reality due to the limited resolution. The relative densities of 99.3±0.09 % (not sintered) and 98.4±0.04 % (sintered) determined by the

Archimedean method show only a doubling of the porosity of the precursor to 1.6 % after sintering.

3.3 Influence of Blowing Agent

Fig. 9 shows the comparison between an AlSi8Mg4 sample containing 0.25 wt% TiH_2 (blue curves) as blowing agent and one without (black curves) foamed at 620 °C, tomoscopically acquired at 1 Hz at the TOMCAT beamline. **Fig. 9a** shows the bubble density (dotted) and the development of porosity. In **Fig. 9b**, the mean equivalent bubble diameters, derived from the maximum of the underlying normal distribution of the volume-weighted bubble diameters with the standard deviations as error bars, are shown for the first stage. Tomographic sections at the indicated time are shown in **Fig. 9c**.

Two-stage bubble formation occurs in both systems. With blowing agent, it develops more nucleating bubbles (1697 mm^{-3} at 27 s to 999 mm^{-3} at 26 s) in the first stage, which can also be qualitatively observed in the images, but also decreases more strongly until the transition to the second stage (reduction by 429 mm^{-3}/25 % compared with 120 mm^{-3}/12 %). In the second bubble development stage, the bubble number density for the sample with blowing agent increases slightly more to 2691 mm^{-3} at 44 s against 2372 mm^{-3} at 45 s, but also decreases more thereafter, with a stronger decrease from about 60 s reaching 73 % less bubbles than for the blowing agent free sample. With added blowing agent the porosity is at higher values until the end of the first range (up to 40 s), in the second stage it rises approximately in a similar way up to 30 % and from about 60 s, with a progressive reduction of the number of bubbles, it rises faster to final values of 80 % whereas the sample without blowing agent remains below 50 % porosity. The average bubble size in the first bubble formation stage is initially similar but increases more with the blowing agent after the first bubble number maximum has been exceeded, while the distribution widens. As can be seen in the upper tomographic image (**Fig. 9c**) of the sample with TiH_2 (framed in blue), for the first bubble formation stage, no spatial correlation was observed between the bubbles formed and the highly absorbent blowing agent particles.

4. Discussion

4.1 Adsorbates and first stage of nucleation

The powder metallurgical process for the production of metal foams offers many possibilities for optimisation through the interaction of various parameters during the pressing of the precursor and foaming, and even in the selection of the powders. One important parameter is the type and amount of blowing agent, usually TiH_2. Furthermore, it was found that Al-based precursors and especially those containing Mg-rich components or powders exposed to ambient humidity during pressing [42] contain gas adsorbed on the metallic powder surfaces and allow gas nucleation and even foaming under ambient pressure without additional blowing agent just by adding AlMg50 master alloy powder, which leads to homogeneous foam structures due to the uniform gas distribution and small pressure differences between the bubbles [18,43,44]. Decomposition of adsorbates (mostly physisorbed water and hydroxides) on the powder surface, e.g.: aluminium hydroxide, leads to the release of water ($2Al(OH)_3 \rightarrow Al_2O_3 + 3H_2O$) which oxidises Al to form hydrogen ($2Al + 3H_2O \rightarrow Al_2O_3 + 3H_2$) [45]. In the temperature range up to 200 °C, mainly water is desorbed. At higher temperatures, hydroxides are decomposed, which leads to an increasing hydrogen release from about 300 °C onward, with a maximum between 400 °C and 500 °C [45,46].

The evolution of the number of bubbles and of the porosity of all AlSi8Mg4 samples considered in this work takes place in clearly distinguishable stages. In the first, which begins at about ~450 °C, and coincides with the melting temperature of the Al-Mg phases (T_m(β-Al_3Mg_2) = 450 °C / T_m(γ-$Al_{12}Mg_{17}$) = 459 °C [33]) in the AlMg50 alloy mixed into the precursors, small (most below 100 µm in diameter), round (Ψ ~ 0.8) bubbles are formed, that are well distributed over the whole sample as the gas coming from the adsorbates is well distributed (see **Figs. 3** and **4**). A clear correlation of bubble nucleation with the location of the former AlMg50 particles has been found (see **Figs. 3, 5, 6, 8** and **9**). A small number of bubbles of low sphericity of 0.4 (on the left side of **Fig. 4a**), which are located near the edge of the observed volume, are also initially detected here and are attributable to cavities that have been created by melt ejection at the sample surface and extend into the observation volume. They adopt the shape of the former AlMg50 powder particles. This can also be seen in the upper part of the first tomographic sectional image in **Fig. 6**. The molten areas are ejected as small liquid droplets from the remaining still solid precursor. This phenomenon can be observed in **Fig. A.3** and in the second column of **Fig. A.4** for all alloys with large AlMg50 particles. Some of these external melt droplets even contain gas bubbles, which supports the assumption that gas nucleates in this early molten phase. This can have a positive effect on the integrity of the precursor and, as a kind of buffer, can prevent tearing due to excessive gas pressures. A similar effect was found for precursors with added zinc [47].

No large bubble volume develops at this temperature, as porosity is mostly <10 % and is caused by adsorbates as the main gas source in this stage, which is well distributed but yields a limited total gas volume. A proof of this can be observed in **Fig. A.4** for sieved and unsieved AlMg50 powder additions, where finer or coarse powders lead to a lower or higher foam density, respectively, and was also reported in the literature [48]. For the alloy AlSi8Mg4 investigated here, notable porosities could also be achieved during foaming without additional blowing agent (see **Fig. 9**) [49].

4.2 Second nucleation and full melting

At about 560 °C, the second nucleation stage takes place, which is caused by the sudden formation of a large amount (around 50 % initially with a rapid rise to 100 % within ~40 K) of liquid phase (ternary AlMgSi with T_m = 557 °C) and to some extent the increasing release of hydrogen by the blowing agent TiH_2 [15,17]. This is observed in **Fig. 4** by the sudden distribution broadening with a jump in bubble sphericity, when the bubbles connect through the developing melt network. The counterpressure generated by the structural integrity drops, therefore existing bubbles can expand, leading to a sudden increase in porosity. By lowering the nucleation barrier, the bubble density increases due to newly generated bubbles in a short period of time (see **Figs. 3, 6** or **9**). The bubble density has a maximum shortly after at ~580 °C, but decreases then, although the porosity further increases (**Figs. 3, 6** and **9**) until the sample has completely melted (**Fig. 6**), faster than reported previously [17]. This is caused by the limited and constant volume observed here, and can be explained first by a reduction of the nucleation rate, as gas does not need to further nucleate and can now more easily diffuse to already existing bubbles due to the increased porosity, but mainly due to bubble coalescence in the course of further foam expansion, as also indicated in **Fig. 9** for the comparison of samples with and without blowing agent [17,50].

4.3 Role of blowing agent

Although using a blowing agent such as TiH_2 increases the final porosity, it is unfavourable for obtaining fine bubbles and a large bubble density in the final foam (see **Fig. 9**) due to increased coalescence caused by an inhomogeneous gas pressure distribution [51]. Consequently, TiH_2 is to a certain extent also detrimental for a large foam expansion and a homogeneous final pore structure of the solid foam. When the liquid films become unstable or the pressure difference built up by the gas sources becomes too high and first coalescence occurs among nearby bubbles, some bubbles grow faster and the distribution broadens. This occurs earlier and faster than in samples without blowing agent due to the additional pressure of the more local and intense gas source of added blowing agent particles. In this case the additional gas volume increases the pressure and also causes more nucleation centres [22], which is reflected also in the bubble density in **Fig. 9**.

4.4 Microstructure dependence

In addition to the gas source (adsorbates or blowing agent), a further knob for an adjustment of a preferred structure of the foam is a specific modification of the precursor microstructure, e.g., the particle size of the AlMg50 master alloy. A comparison between unsieved and sieved powders is shown in **Fig. A.4** and **Table A.1**. Both large and small AlMg50 particles can lead to low bubble counts. Large particles cause a large amount of melt to discharge at the surface of the sample (**Fig. A.4**, second column). Due to the preferred gas nucleation in the AlMg particles, the distribution of nucleation centres is rather inhomogeneous in samples with large particles. Due to the more homogeneously distributed small particles, which are faster alloyed by the pressing process, complete melting is faster, which leads to an early large expansion already in the heating stage (**Fig. A.4**, second row). However, a melt network is more likely to develop, which allows bubbles to merge over a large range

(**Fig. A.4**, third column). The liquid films are thicker, longer, and more stable due to the higher number of oxides in the powders (**Fig. A.4**, fifth column), which together with the increasing gas release from the blowing agent can result in bursting and instabilities in the growth stage. The highest foam stability (~6 % shrinkage) with acceptable expansion (>4.7 V/V_0) is shown by the sieved powder size fraction (40–100) µm (**Fig. A.4**, third row).

Hot compacting at 400 °C changes the microstructure of the powder compact, which is reflected for example in the formation of a β-Al_3Mg_2 boundary layer (Samson phase [52], also known as $Al_{63}Mg_{37}$, Al_8Mg_5 or $Al_{140}Mg_{89}$ [53], with a slightly variable composition between ~35 wt% and 38 wt% Mg) in the AlMg50 particles at the interface between γ phase and Al matrix (see **Figs. 7** and **8**). This core-shell structure (with an average shell thickness of 25 µm for samples compacted for 15 min at 400 °C/300 MPa) cannot be directly detected in tomography because of the low X-ray absorption difference between β and γ phase. Also, the available X-ray phase contrast caused by the interface between both phases is too low due to the polychromatic radiation and short exposure times employed here. However, a slight shading (as seen in **Fig. 8** in the large particles on the left side) is indeed indicative of the presence of that core shell structure. On the other hand, **Fig. 6** verifies the presence of Mg_2Si formed in the precursor and shows the disappearance of γ and β phase and the growth of Mg_2Si at lower temperatures. Particles with an equivalent diameter below 150 µm present a reduced γ core or even only β phase due to their predominantly flat shapes. An accumulation of bubble formation in the boundary region of the AlMg50 particles could be detected. Taking into account the particle size distribution of AlMg particles determined from the tomograms (**Fig. A.2**), the 25-µm thick boundary layer accounts for about 69 vol% of all particles and thus 2.4 vol% of the considered sample volume, which corresponds to about 40 times the nucleation density and demonstrates that nucleation takes place there. The average distance accumulation of the bubbles from the particles surface between 10–20 μm indicates the preference of bubbles to nucleate and grow in the shell. This can be explained on the one hand by the approximately 10 K lower melting point of the β shell (450 °C) compared to the γ core (459 °C). The transformation of the γ phase to β during compaction can also lead to local porosity development in the precursor due to its lower Mg content causing a decrease in hydrogen solubility and the theoretical hydrogen capacity bound as MgH_2 (from 4.4 wt% to 3 wt%) [54]. Mg_2Si forms between AlMg50 and Si particles during the compaction of the powder (**Fig. 7**). After sintering of the pressed precursors, its content increases (**Fig. 8**). It is very hard and high melting (melting temperature 1076 °C [55]) and could serve as starting points for gas accumulation (heterogeneous nucleation) [56] similar to the case of pure Si particles in AlSi foams [11], which can already be seen in the increase in porosity after sintering at 400 °C.

The local restriction of bubble nucleation to the already molten, small areas leads to high local bubble density and early bubble coalescence, as shown in **Fig. 5** and determined by the decrease in bubble density in **Figs. 3** and **9**. The broadening of the bubble size distribution and the lower sphericity observed in **Fig. 4** until 556 °C can be explained by the coalescence of the existing bubbles before some fill in the former particle's shape. This has already been shown for similar microstructure constellations [18].

The temporal evolution of the diffracted intensities (**Fig. 6**) not only shows that the maximum bubble number coincides with the main melt formation (represented by a strong background scattering of the non-crystalline melt). The lattice parameter derived from the positions of the diffracted reflexes of the phases involved can also tell us something about the dynamic alloy formation process (**Fig. 10**). Assuming that the lattice parameter of Si changes only thermally, since it does not form a solid solution with other elements involved, a non-trivial behaviour can be observed for the Al reflections. I) Initially, the lattice parameter increases more strongly than when taking thermal expansion into account [57]. II) The slope decreases from about 200 °C and ascends analogously between 300 °C and 450 °C, but is shifted to 0.4 pm higher values than for pure Al, which corresponds to a dissolved Mg content of about 1 wt% [33]. III) After that, the lattice parameter continues to rise even faster to 1 pm above the value for pure Al, which corresponds to about 2 wt% dissolved Mg. This can be explained by the resulting, more reactive AlMg melt, and the corresponding Mg diffusion into the Al matrix. IV) Until melting, the lattice constant converges again and thus represents the residual fraction of little to unalloyed aluminium. During cooling (blue symbols) the lattice parameter shows a different course. Until about 450 °C it decreases analogously to the thermal contraction at slightly higher values, corresponding to a Mg content of 1 wt% and then decreases less strongly to a value of 2 pm above the reference curve. This corresponds approximately to the original admixed amount of 4 wt% Mg. This value is somewhat high, since Mg also reacts with Si to form Mg_2Si. Further influences, e.g. the distortion of the lattice by the orientation of the Al grains, which are large in relation to the cell walls, or eutectic transformation must be taken into account here, but the course shows that the interaction of the precursor components is complex and that the dynamics of foaming can be influenced by their composition.

Despite all advantages of the alloy AlSi8Mg4 already mentioned in the introduction, the understanding and improving of the gas nucleation stage remains a crucial step for the further structural development of the foam to improve properties for applications. A very large influence is provided by the microstructure of the precursor, which is determined by the compaction parameters, but especially by the properties of the underlying powder and should therefore be further investigated.

5. Conclusions

- Nucleation and growth steps of gas bubbles of the AlSi8Mg4 system were studied in detail with X-ray tomoscopy.
- The first nucleation stage is very homogeneous, with low porosity and spherical bubbles formed. Adsorbates were identified as main gas source. No local correlation of nucleation points with TiH_2, but with AlMg50 particles was found (formation of bubbles coincides with the disappearance/melting of the AlMg-β-phase during foaming and formation of Mg_2Si and microporosity during sintering).
- Early bubble coalescence was found due to the limited nucleation volume. The first nucleation stage takes place in the outer shell (consisting of β phase) of the AlMg50 particles, which further limits the space available for bubble growth.
- Melt ejection reflects the effect of first nucleation and early melt fraction at the surface.
- The second nucleation stage is abrupt and inhomogeneous, attributed to the melting of the alloy and the fast formation of a large amount of liquid phase.
- A pronounced foam aging stage with bubble growth, coalescence and rounding up of bubbles was observed following the second bubble formation stage.
- The added blowing agent influences mainly the foam growth and aging (coalescence) stage.
- Strong influence of AlMg50 powder particle size on the nucleation and formation of foam structure (surface, oxides, gas amount and distribution, γ to β ratio) was confirmed showing potential for improvement, for example by selecting suitable powder sizes and possible pre-treatment or pre-alloying of the powders.

Acknowledgements

The authors would like to acknowledge Christian Matthias Schlepütz and Rajmund Mokso for their support at the TOMCAT beamline and Manuela Klaus and Daniel Apel for their support with the diffraction setup at the EDDI beamline. We thank Helmholtz-Zentrum Berlin, Germany for the allocation of synchrotron radiation beamtime for the commissioning of the tomography setup at the EDDI beamline of BESSY II. We acknowledge the Paul Scherrer Institut, Villigen, Switzerland for provision of synchrotron radiation beamtime at the TOMCAT beamline of the SLS as part of the long-term project 20170886. This research was supported by the Deutsche Forschungsgemeinschaft, DFG, project numbers 282420267 and 408321454.

References

[1] M.A. De Meller, Produit métallique pour l’obtention d’objets laminés, moulés ou autres, et procédés pour sa fabrication, French Patent 615.147, 1926.

[2] F. García-Moreno, Commercial applications of metal foams: Their properties and production, Materials (Basel). 9 (2016). https://doi.org/10.3390/ma9020085.

[3] J. Banhart, Manufacture, characterisation and application of cellular metals and metal foams, Prog. Mater. Sci. 46 (2001) 559–632. https://doi.org/10.1016/S0079-6425(00)00002-5.

[4] F. García-Moreno, C. Jiménez, M. Mukherjee, P. Holm, J. Weise, J. Banhart, Experiments on metallic foams under gravity and microgravity, Colloids Surfaces A Physicochem. Eng. Asp. 344 (2009) 101–106. https://doi.org/10.1016/j.colsurfa.2009.03.010.

[5] E. Andrews, W. Sanders, L.J. Gibson, Compressive and tensile behaviour of aluminum foams, Mater. Sci. Eng. A. 270 (1999) 113–124. https://doi.org/10.1016/S0921-5093(99)00170-7.

[6] J.L. Grenestedt, On interactions between imperfections in cellular solids, J. Mater. Sci. 40 (2005) 5853–5857. https://doi.org/10.1007/s10853-005-5019-4.

[7] X. Yang, W. Wang, L. Yan, Q. Zhang, T.J. Lu, Effect of pore morphology on cross-property link for close-celled metallic foams, J. Phys. D. Appl. Phys. 49 (2016). https://doi.org/10.1088/0022-3727/49/50/505301.

[8] F. García-Moreno, M. Jürgens, J. Banhart, Temperature dependence of film rupture and internal structural stability in liquid aluminium alloy foams, Acta Mater. 196 (2020) 325–337. https://doi.org/10.1016/j.actamat.2020.06.054.

[9] S.N. Sahu, A.A. Gokhale, A. Mehra, Modeling nucleation and growth of bubbles during foaming of molten aluminum with high initial gas supersaturation, J. Mater. Process. Technol. 214 (2014) 1–12. https://doi.org/10.1016/j.jmatprotec.2013.07.009.

[10] C.C. Yang, H. Nakae, The effects of viscosity and cooling conditions on the foamability of aluminum alloy, J. Mater. Process. Technol. 141 (2003) 202–206. https://doi.org/10.1016/S0924-0136(02)01048-8.

[11] A. Rack, H.M. Helwig, A. Bütow, A. Rueda, B. Matijašević-Lux, L. Helfen, J. Goebbels, J. Banhart, Early pore formation in aluminium foams studied by synchrotron-based microtomography and 3-D image analysis, Acta Mater. (2009). https://doi.org/10.1016/j.actamat.2009.06.045.

[12] H.M. Helwig, S. Hiller, F. García-Moreno, J. Banhart, Influence of compaction conditions on the foamability of AlSi8Mg4 alloy, Metall. Mater. Trans. B Process Metall. Mater. Process. Sci. 40 (2009) 755–767. https://doi.org/10.1007/s11663-009-9264-9.

[13] L. Helfen, T. Baumbach, H. Stanzick, J. Banhart, A. Elmoutaouakkil, P. Cloetens, Viewing the early stage of metal foam formation by computed tomography using synchrotron radiation, Adv. Eng. Mater. 4 (2002) 808–813. https://doi.org/10.1002/1527-2648(20021014)4:10<808::AID-ADEM808>3.0.CO;2-U.

[14] H.M. Helwig, F. García-Moreno, J. Banhart, A study of Mg and Cu additions on the foaming behaviour of Al-Si alloys, J. Mater. Sci. 46 (2011) 5227–5236. https://doi.org/10.1007/s10853-011-5460-5.

[15] F. García-Moreno, L.A. Radtke, T.R. Neu, P.H. Kamm, M. Klaus, C.M. Schlepütz, J. Banhart, The influence of alloy composition and liquid phase on foaming of Al–Si–Mg alloys, Metals (Basel). 10 (2020). https://doi.org/10.3390/met10020189.

[16] F. García-Moreno, C. Jiménez, P.H. Kamm, M. Klaus, G. Wagener, J. Banhart, C. Genzel, White-beam X-ray radioscopy and tomography with simultaneous diffraction at the EDDI beamline, J. Synchrotron Radiat. 20 (2013) 809–810. https://doi.org/10.1107/S0909049513018670.

[17] F. García-Moreno, P.H. Kamm, T.R. Neu, F. Bülk, R. Mokso, C.M. Schlepütz, M. Stampanoni, J. Banhart, Using X-ray tomoscopy to explore the dynamics of foaming metal, Nat. Commun. 10 (2019). https://doi.org/10.1038/s41467-019-11521-1.

[18] P.H. Kamm, F. García-Moreno, T.R. Neu, K. Heim, R. Mokso, J. Banhart, Fast Synchrotron X-Ray Tomography of Dynamic Processes in Liquid Aluminium Alloy Foam, Adv. Eng. Mater. 19 (2017) 1600550.

https://doi.org/10.1002/adem.201600550.

[19] C. Jiménez, M. Paeplow, P.H. Kamm, T.R. Neu, M. Klaus, G. Wagener, J. Banhart, C. Genzel, F. García-Moreno, Simultaneous X-ray radioscopy/tomography and energy-dispersive diffraction applied to liquid aluminium alloy foams, J. Synchrotron Radiat. 25 (2018) 1790–1796. https://doi.org/10.1107/S1600577518011657.

[20] A.R. Kennedy, V.H. Lopez, The decomposition behavior of as-received and oxidized TiH_2 foaming-agent powder, Mater. Sci. Eng. A. 357 (2003) 258–263. https://doi.org/10.1016/S0921-5093(03)00211-9.

[21] B. Matijasevic, S. Fiechter, I. Zizak, O. Görke, N. Wanderka, P. Schubert-Bischoff, J. Banhart, Decomposition behaviour of as-received and oxidized TiH_2 powder, in: Proc. PM2004 Powder Metall. World Congr. Vienna, Vol. 4 Eur. Powder Metall. Assoc. Shrewsbury, 2004: pp. 149–154.

[22] C. Jiménez, F. García-Moreno, B. Pfretzschner, M. Klaus, M. Wollgarten, I. Zizak, G. Schumacher, M. Tovar, J. Banhart, Decomposition of TiH2 studied in situ by synchrotron X-ray and neutron diffraction, Acta Mater. 59 (2011) 6318–6330. https://doi.org/10.1016/j.actamat.2011.06.042.

[23] W. van Aarle, W.J. Palenstijn, J. Cant, E. Janssens, F. Bleichrodt, A. Dabravolski, J. De Beenhouwer, K. Joost Batenburg, J. Sijbers, Fast and flexible X-ray tomography using the ASTRA toolbox, Opt. Express. 24 (2016) 25129–25147. https://doi.org/10.1364/oe.24.025129.

[24] F. Marone, M. Stampanoni, Regridding reconstruction algorithm for real-time tomographic imaging, J. Synchrotron Radiat. 19 (2012) 1029–1037. https://doi.org/10.1107/S0909049512032864.

[25] R. Mokso, C.M. Schlepütz, G. Theidel, H. Billich, E. Schmid, T. Celcer, G. Mikuljan, L. Sala, F. Marone, N. Schlumpf, M. Stampanoni, GigaFRoST: The gigabit fast readout system for tomography, J. Synchrotron Radiat. 24 (2017) 1250–1259. https://doi.org/10.1107/S1600577517013522.

[26] J.L. Fife, M. Rappaz, M. Pistone, T. Celcer, G. Mikuljan, M. Stampanoni, Development of a laser-based heating system for in situ synchrotron-based X-

ray tomographic microscopy, J. Synchrotron Radiat. 19 (2012) 352–358. https://doi.org/10.1107/S0909049512003287.

[27] J. Schindelin, I. Arganda-Carreras, E. Frise, V. Kaynig, M. Longair, T. Pietzsch, S. Preibisch, C. Rueden, S. Saalfeld, B. Schmid, J.Y. Tinevez, D.J. White, V. Hartenstein, K. Eliceiri, P. Tomancak, A. Cardona, Fiji: An open-source platform for biological-image analysis, Nat. Methods. 9 (2012) 676–682. https://doi.org/10.1038/nmeth.2019.

[28] I.T. Jolliffe, Principal Component Analysis, Second Edi, Springer New York, 2002. https://doi.org/10.2307/1270093.

[29] H. Wadell, Sphericity and Roundness of Rock Particles, J. Geol. 41 (1933) 310–331. https://doi.org/10.1086/624040.

[30] E.D. Sneed, R.L. Folk, Pebbles in the Lower Colorado River, Texas a Study in Particle Morphogenesis, J. Geol. 66 (1958) 114–150. https://doi.org/10.1086/626490.

[31] M. Klaus, F. García-Moreno, The 7T-MPW-EDDI beamline at BESSY II, J. Large-Scale Res. Facil. JLSRF. 2 (2016). https://doi.org/10.17815/jlsrf-2-63.

[32] D. Apel, M. Klaus, C. Genzel, D. Balzar, Rietveld refinement of energy-dispersive synchrotron measurements, Zeitschrift Fur Krist. 226 (2011) 934–943. https://doi.org/10.1524/zkri.2011.1436.

[33] J.L. Murray, The Al-Mg (Aluminum-Magnesium) system, Bull. Alloy Phase Diagrams. 3 (1982) 60–74. https://doi.org/10.1007/BF02873413.

[34] T. Hom, W. Kiszenik, B. Post, Accurate lattice constants from multiple reflection measurements. II. Lattice constants of germanium silicon, and diamond, J. Appl. Crystallogr. 8 (1975) 457–458. https://doi.org/10.1107/s0021889875010965.

[35] J. Dai, Y. Song, R. Yang, Influences of alloying elements and oxygen on the stability and elastic properties of $Mg_{17}Al_{12}$, J. Alloys Compd. 595 (2014) 142–147. https://doi.org/10.1016/j.jallcom.2014.01.171.

[36] S. Samson, E.K. Gordon, The crystal structure of ε-$Mg_{23}Al_{30}$, Acta Crystallogr. Sect. B Struct. Crystallogr. Cryst. Chem. 24 (1968) 1004–1013. https://doi.org/10.1107/s0567740868003638.

[37] M. Feuerbacher, C. Thomas, J.P.A. Makongo, S. Hoffmann, W. Carrillo-Cabrera, R. Cardoso, Y. Grin, G. Kreiner, J.M. Joubert, T. Schenk, J. Gastaldi, H. Nguyen-Thi, N. Mangelinck-Nöel, B. Billia, P. Donnadieu, A. Czyrska-Filemonowicz, A. Zielinska-Lipiec, B. Dubiel, T. Weber, P. Schaub, G. Krauss, V. Gramlich, J. Christensen, S. Lidin, D. Fredrickson, M. Mihalkovic, W. Sikora, J. Malinowski, S. Brühne, T. Proffen, W. Assmus, M. De Boissieu, F. Bley, J.L. Chemin, J. Schreuer, W. Steurer, The Samson phase, β-Mg_2Al_3, revisited, Zeitschrift Fur Krist. 222 (2007) 259–288. https://doi.org/10.1524/zkri.2007.222.6.259.

[38] R.W.G. Wyckoff, Crystal Structures, Second Edi, Interscience Publishers New York, 1963.

[39] M.D. Nersesyan, Synthesis of titanium and zirconium nitrohydrides in combustion regime, Zhurnal Neorg. Khimii. 29 (1984) 860–863.

[40] Y. Okada, Y. Tokumaru, Precise determination of lattice parameter and thermal expansion coefficient of silicon between 300 and 1500 K, J. Appl. Phys. 56 (1984) 314–320. https://doi.org/10.1063/1.333965.

[41] B.L. Henke, E.M. Gullikson, J.C. Davis, X-ray interactions: Photoabsorption, scattering, transmission, and reflection at E = 50-30, 000 eV, Z = 1-92, At. Data Nucl. Data Tables. 54 (1993) 181–342. https://doi.org/10.1006/adnd.1993.1013.

[42] C. Jiménez, F. García-Moreno, J. Banhart, G. Zehl, Effect of relative humidity on pressure-induced foaming (PIF) of aluminium-based precursors, in: MetFoam 2007 - Proc. 5th Int. Conf. Porous Met. Met. Foam., 2008.

[43] M. Mukherjee, F. García-Moreno, C. Jiménez, J. Banhart, Al and Zn foams blown by an intrinsic gas source, Adv. Eng. Mater. 12 (2010) 472–477. https://doi.org/10.1002/adem.201000017.

[44] F. García-Moreno, J. Banhart, Foaming of blowing agent-free aluminium powder compacts, Colloids Surfaces A Physicochem. Eng. Asp. 309 (2007) 264–269. https://doi.org/10.1016/j.colsurfa.2007.03.017.

[45] J.L. Estrada, J. Duszczyk, B.M. Korevaar, Gas entrapment and evolution in prealloyed aluminium powders, J. Mater. Sci. 26 (1991) 1431–1442.

https://doi.org/10.1007/BF00544650.

[46] A. Nylund, I. Olefjord, Degassing of USGA-atomized A15Mn6Cr powder after exposure to a humid atmosphere, Mater. Sci. Eng. A. 134 (1991) 1225–1228. https://doi.org/10.1016/0921-5093(91)90961-L.

[47] A. Ibrahim, C. Körner, R.F. Singer, Investigation of micro pore creation on the PM-foam morphology, in: Cell. Met. Polym., 2004: pp. 61–64.

[48] F. García-Moreno, M. Mukherjee, C. Jiménez, J. Banhart, Pressure-induced foaming of metals, Jom. 67 (2015) 955–965. https://doi.org/10.1007/s11837-015-1331-x.

[49] P.H. Kamm, F. García-Moreno, C. Jiménez, J. Banhart, Suitability of various complex hydrides for foaming aluminum alloys, J. Mater. Res. 28 (2013) 2436–2443. https://doi.org/10.1557/jmr.2013.110.

[50] C. Körner, Foam formation mechanisms in particle suspensions applied to metal foams, Mater. Sci. Eng. A. 495 (2008) 227–235. https://doi.org/10.1016/j.msea.2007.09.089.

[51] F. García-Moreno, E. Solórzano, J. Banhart, Kinetics of coalescence in liquid aluminium foams, Soft Matter. 7 (2011) 9216–9223. https://doi.org/10.1039/c1sm05831b.

[52] S. Samson, The crsytal structure of the phase β Mg_2Al_3, Acta Crystallogr. 19 (1965) 401–413. https://doi.org/10.1107/s0365110x65005133.

[53] M. Mezbahul-Islam, A.O. Mostafa, M. Medraj, Essential Magnesium Alloys Binary Phase Diagrams and Their Thermochemical Data, J. Mater. 2014 (2014) 1–33. https://doi.org/10.1155/2014/704283.

[54] A. Andreasen, Hydrogenation properties of Mg-Al alloys, Int. J. Hydrogen Energy. 33 (2008) 7489–7497. https://doi.org/10.1016/j.ijhydene.2008.09.095.

[55] K.C.H. Kumar, N. Chakraborti, H.-L. Lukas, O. Bodak, L. Rokhlin, Aluminium - Magnesium - Silicon, in: Ternary Alloy Syst. Phase Diagrams, Crystallogr. Thermodyn. Data Light Met. Syst. Part 3 Sel. Syst. from Al-Fe-V to Al-Ni-Zr, 2005: pp. 165–177.

[56] J. Wang, Z. Zhang, Q. Jiang, X. Xia, C. Qiu, J. Ding, W. Zhao, A novel bubble nucleation particle for magnesium composite foam, Mater. Lett. 193 (2017) 187–190. https://doi.org/10.1016/j.matlet.2017.01.103.

[57] P.N.H. Nakashima, The Crystallography of Aluminum and Its Alloys, in: Encycl. Alum. Its Alloy., 2019. https://doi.org/10.1201/9781351045636-140000245.

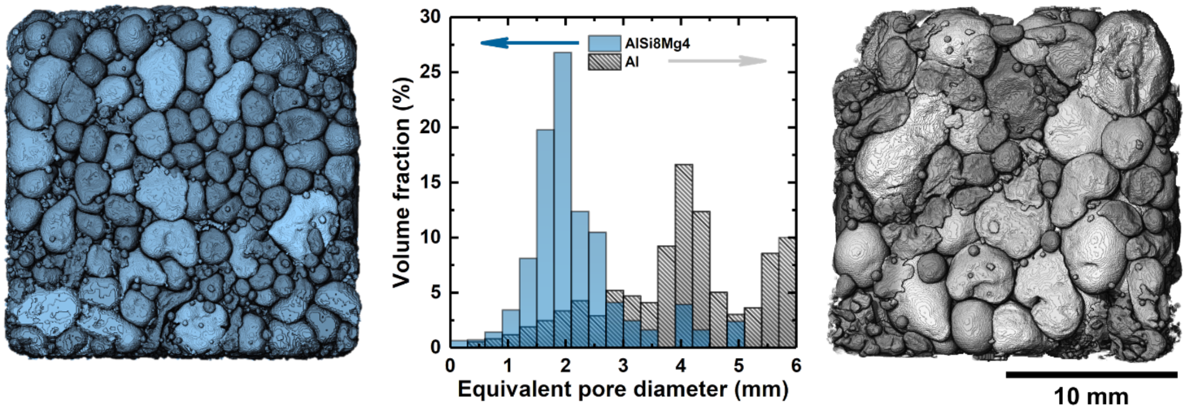

(a) (b) (c)

Fig. 1: Comparison of foamed samples of (a) the alloy AlSi8Mg4 and (c) pure Al with regard to the pore structure stated by their (b) equivalent diameter distributions.

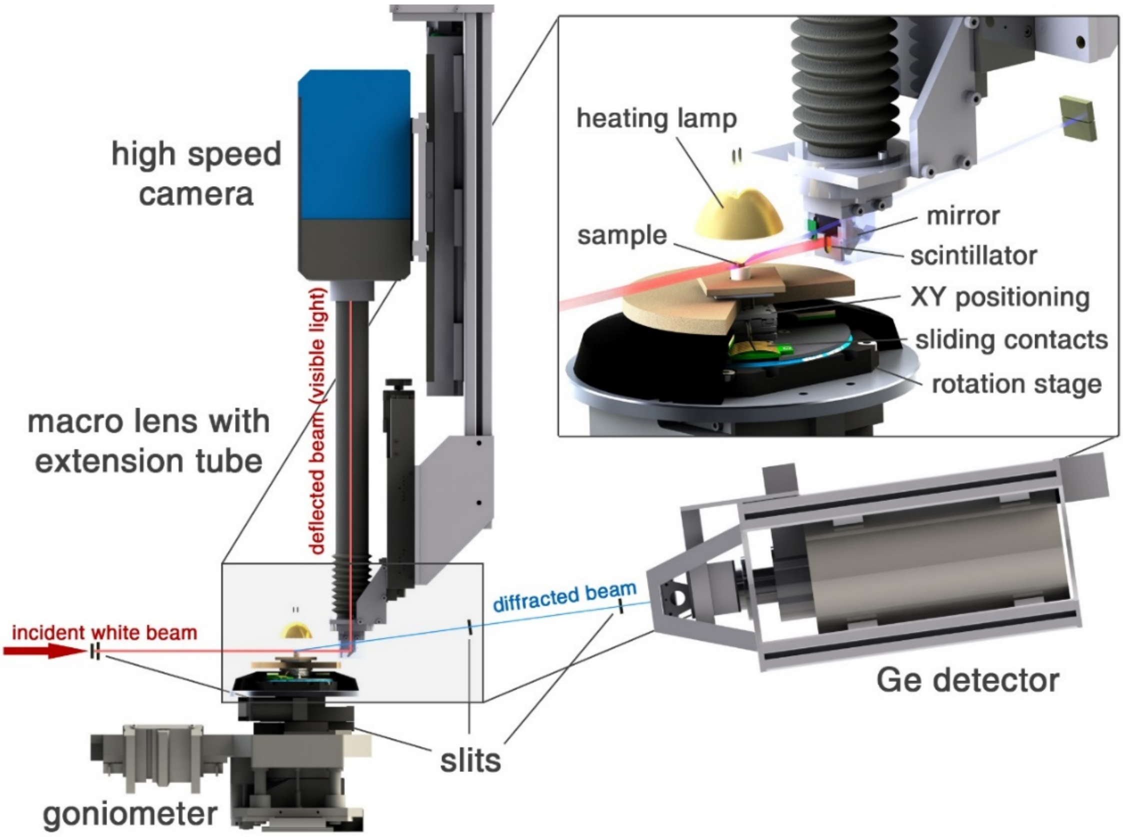

Fig. 2: White beam tomography and simultaneous diffraction setup of the EDDI beamline at BESSY II.

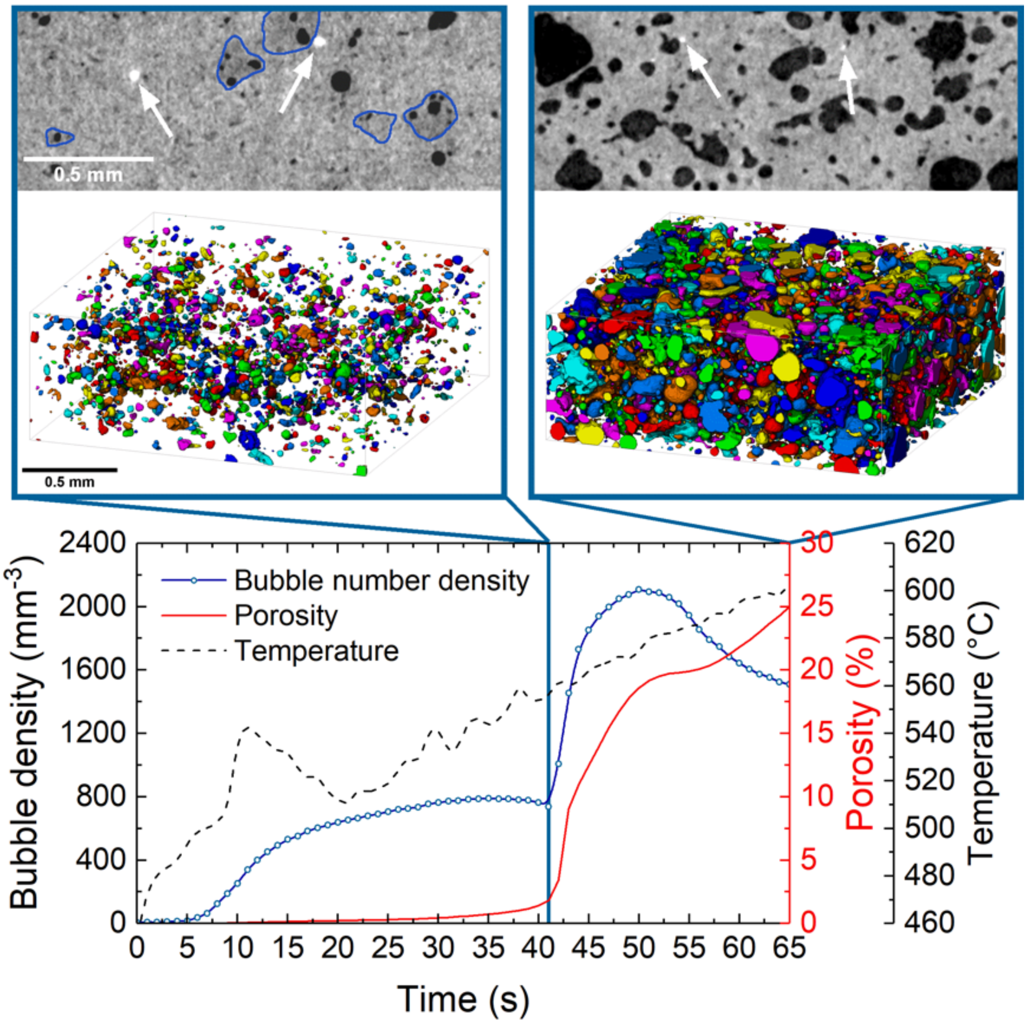

Fig. 3: Early foaming stage (porosity <25 %) of AlSi8Mg4 alloy. Vertical sections through the tomograms and 3D images of the separated bubbles (top) show the moment of the first porosity increase (left pictures, *t* = 41 s) and when the porosity reaches 25 % (right pictures, *t* = 65 s). The graph below shows the temperature curve as well as the bubble density and porosity over the experiment time.

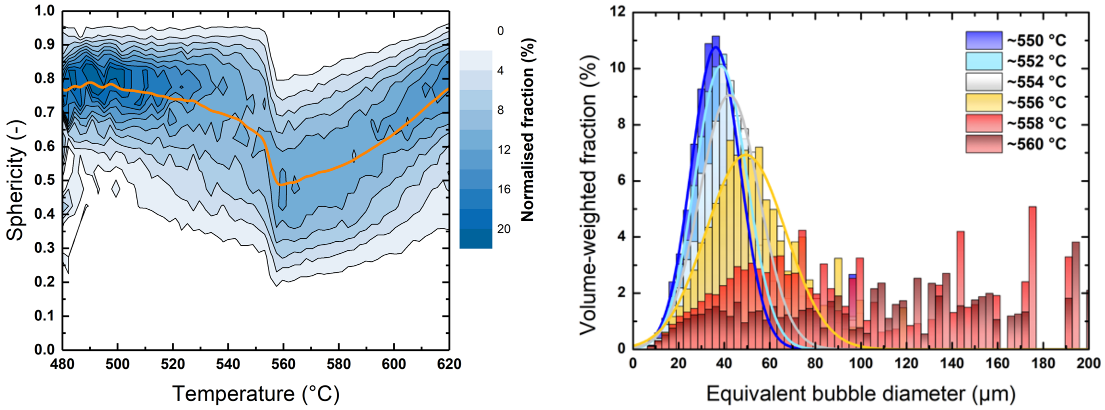

(a) (b)

Fig. 4: (a) Distribution of bubble sphericity in the AlSi8Mg4 sample from Figure 3 versus the foaming temperature and (b) bubble size distributions during the abrupt sphericity transition (550–560 °C) when entering the second bubble formation stage.

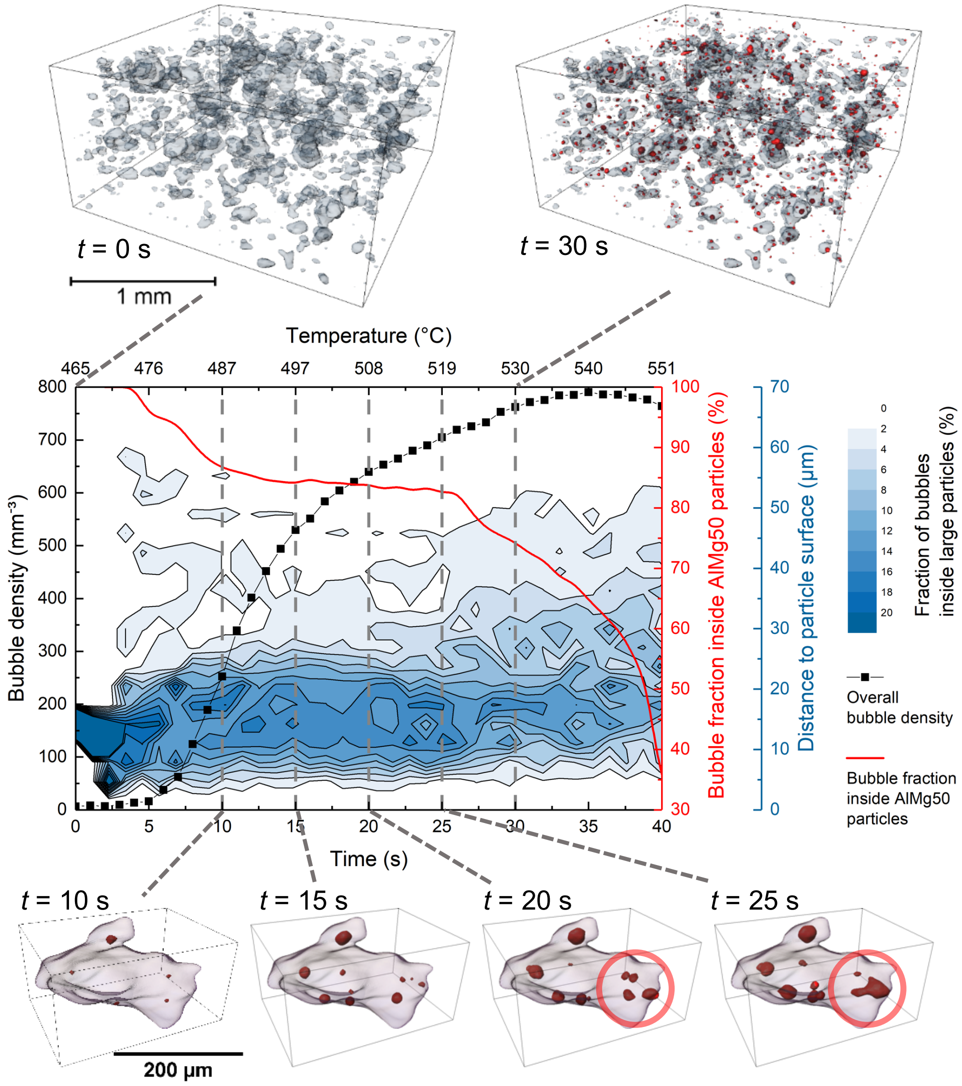

Fig. 5: Centre: Fraction of bubbles nucleated inside AlMg50 particles within the AlSi8Mg4 sample (red curve), bubble density (black, from Fig. 3) and distribution of the distances of bubbles embedded in large AlMg50 particles to the respective particle surface (blue scale coded). Top: 3D representation of the particles (grey) and bubbles (red) at times 0 s (left) and 30 s (right) for the observation volume. Bottom: Representation of an exemplary single AlMg50 particle with internal bubbles at different times.

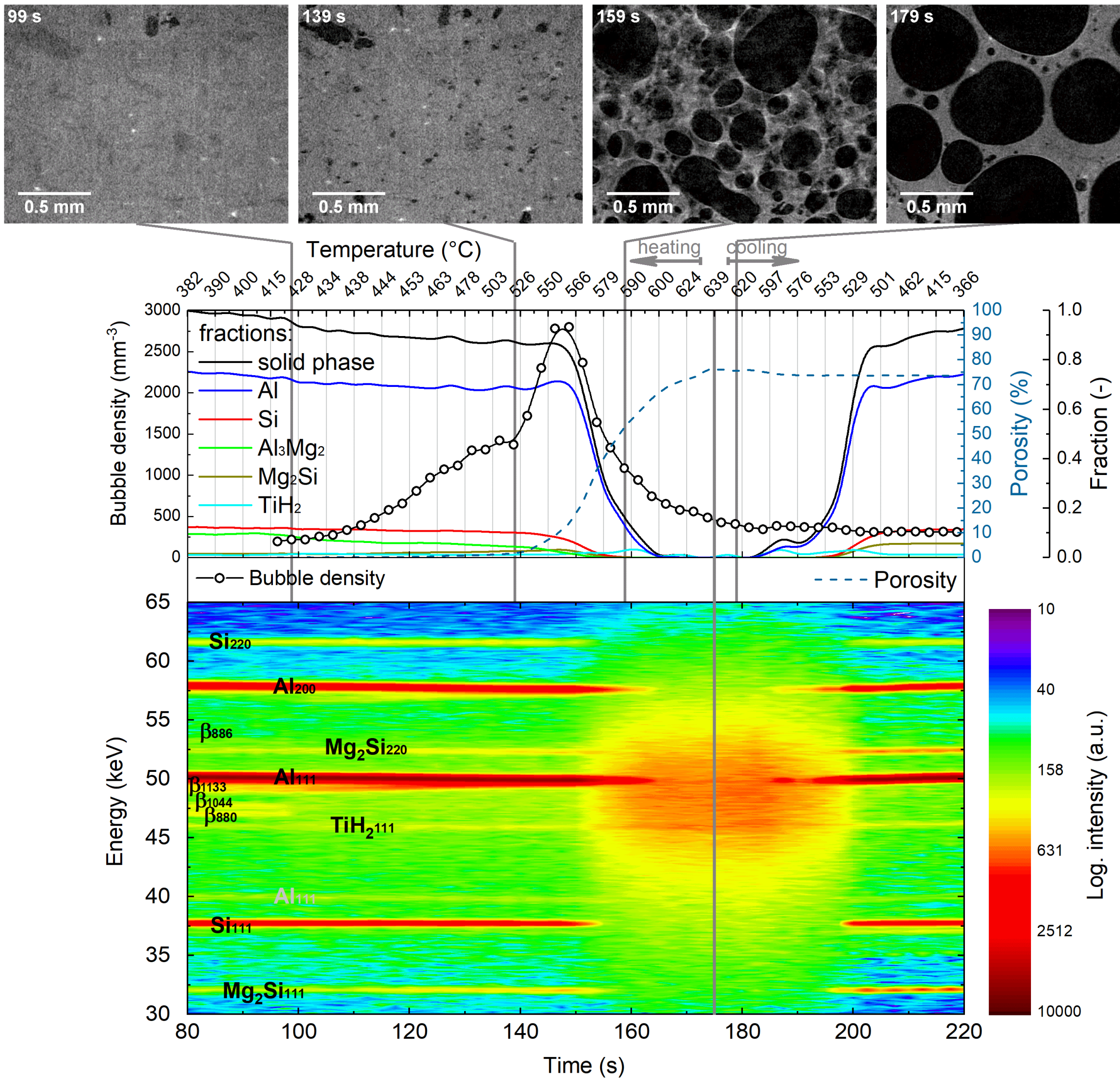

Fig. 6: Time-resolved intensity spectra of the beam energies diffracted by the AlSi8Mg4 sample during foaming conducted by heating the precursor and subsequent naturally cooling (bottom). The determined porosity, bubble density and the fractions of determined phases calculated from the peak areas are displayed over the temperature (above). Tomographic slices show the foam development at selected points in time (top).

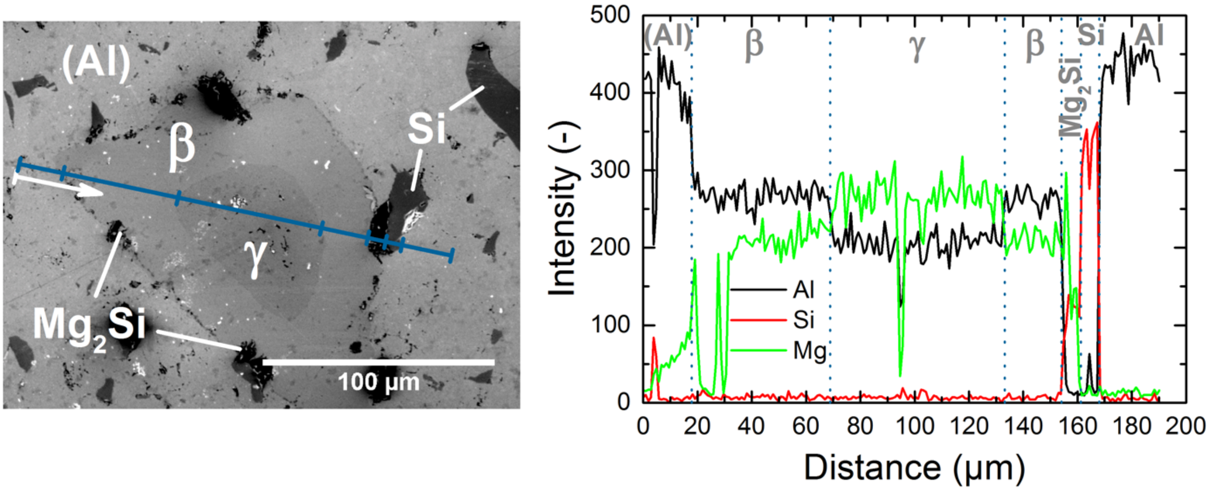

(a) (b)

Fig. 7: (a) Secondary electron SEM image of a precursor of AlSi8Mg4 after hot compaction showing a former AlMg50 particle in the microstructure and (b) EDX line scan measurement depicting the actual elemental composition of Al, Si and Mg.

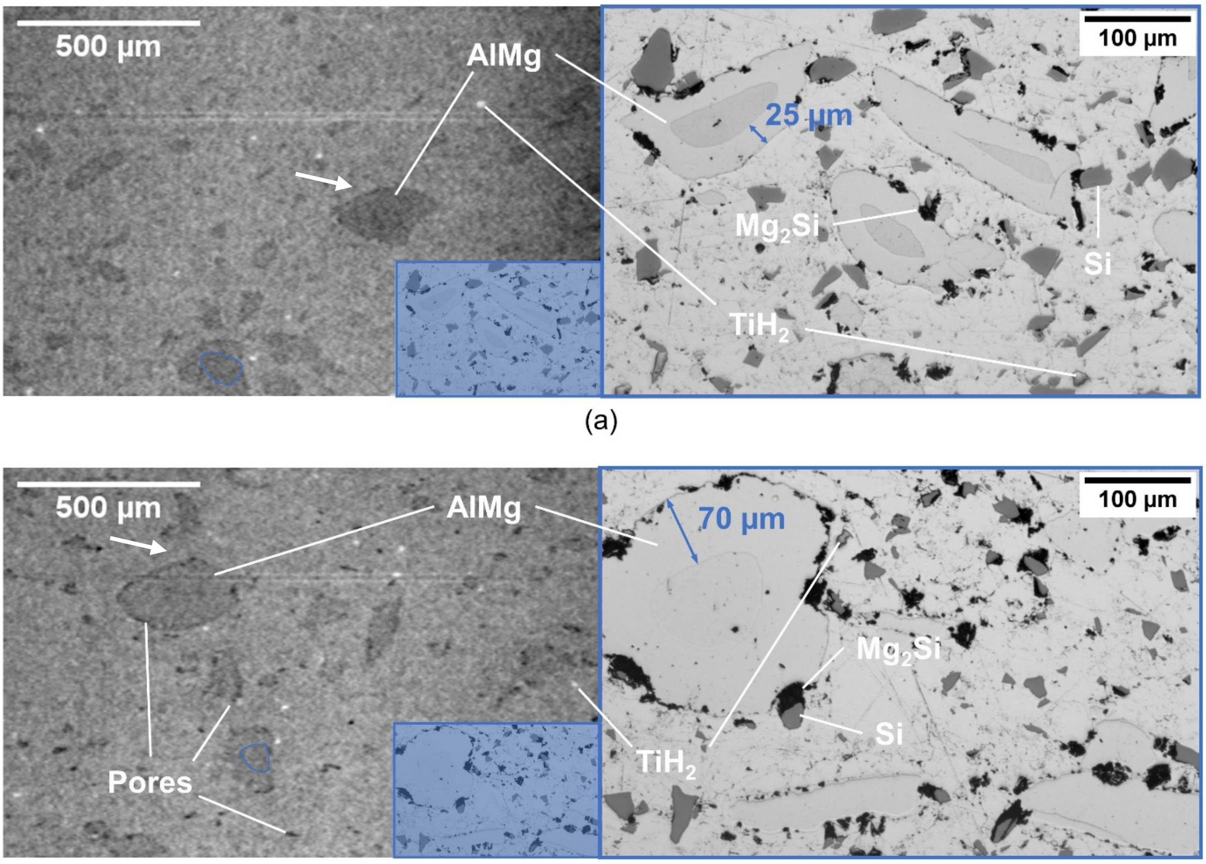

(a)

(b)

Fig. 8: X-ray tomographic slices (left) and light microscopic images (right) of an AlSi8Mg4 precursor (a) after compaction and (b) after subsequent sintering for 1 h at 400 °C.

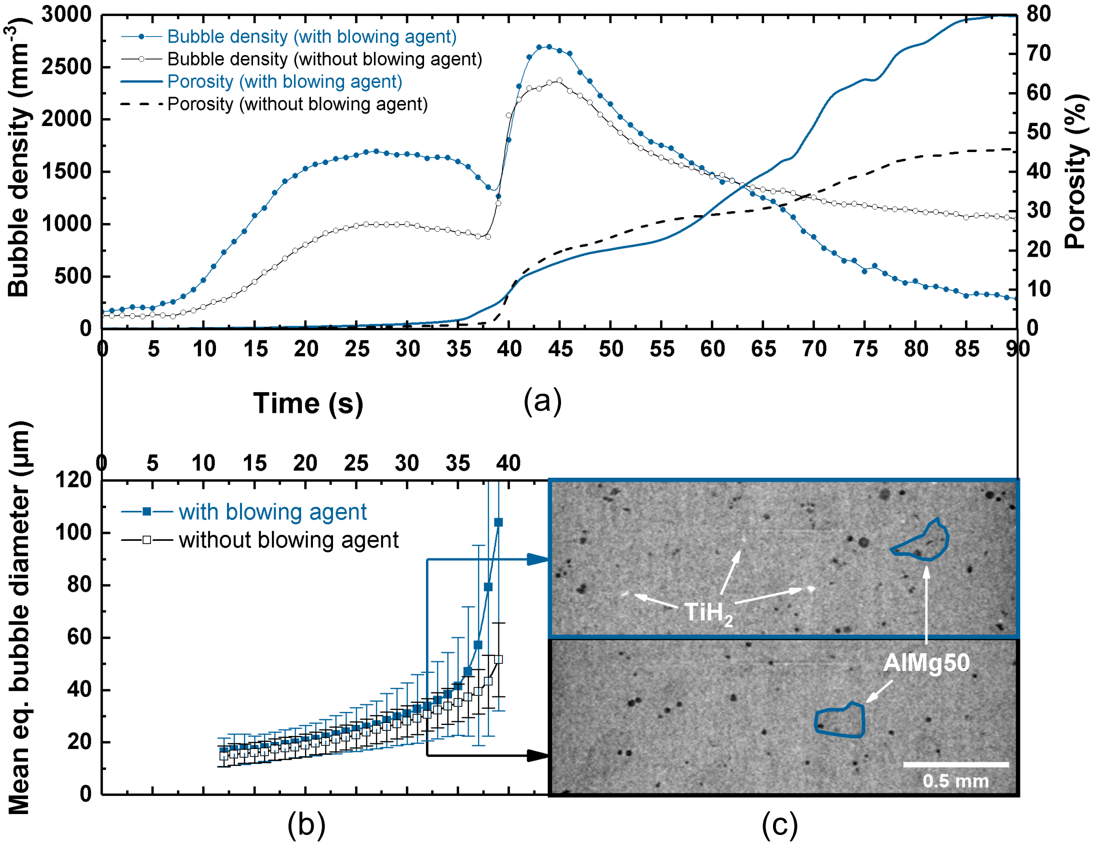

Fig. 9: Comparison of (a) bubble density and porosity evolution, (b) mean equivalent bubble diameter between AlSi8Mg4 with 0.25 wt% TiH_2 and the same alloy without blowing agent addition and (c) vertical tomographic slices taken after 32 s.

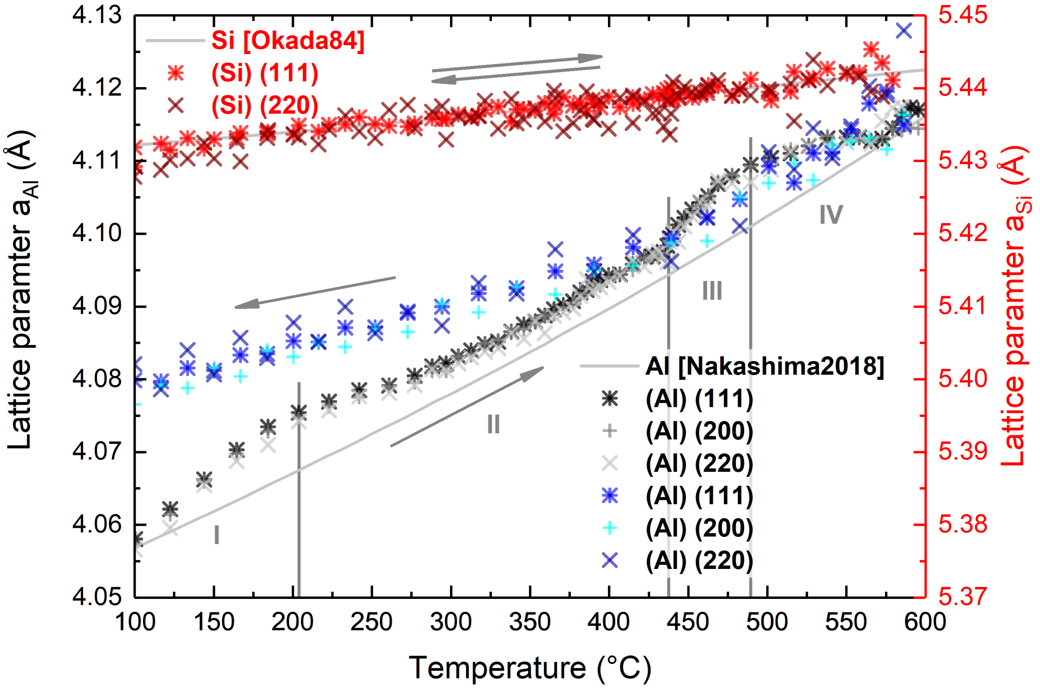

Fig. 10: Lattice parameter of Al calculated from the diffracted energies of the {111} and {200} lattice planes during heating and foaming (black/dark grey) of the sample and cooling (blue/cyan) of the foam compared to literature values (light grey) after calibration of the energy spectrum to literature values for Si (red).

Table 1: List of powders used for alloy preparation as measured by laser diffraction.

Powder	**Supplier**	**Purity (wt%)**	**D_{10} (µm)**	**D_{50} (µm)**	**D_{90} (µm)**
Al	AMG Alpoco UK Ltd.	99.7	20	64	152
Si	Elkem AS	97.5	4	27	60
AlMg50	Possehl Erzkontor GmbH	99.5	21	86	198
Mg	Carl-Roth GmbH	99.8	23	48	81
TiH_2	Chemetall GmbH	98.8	3	14	33

Appendix A

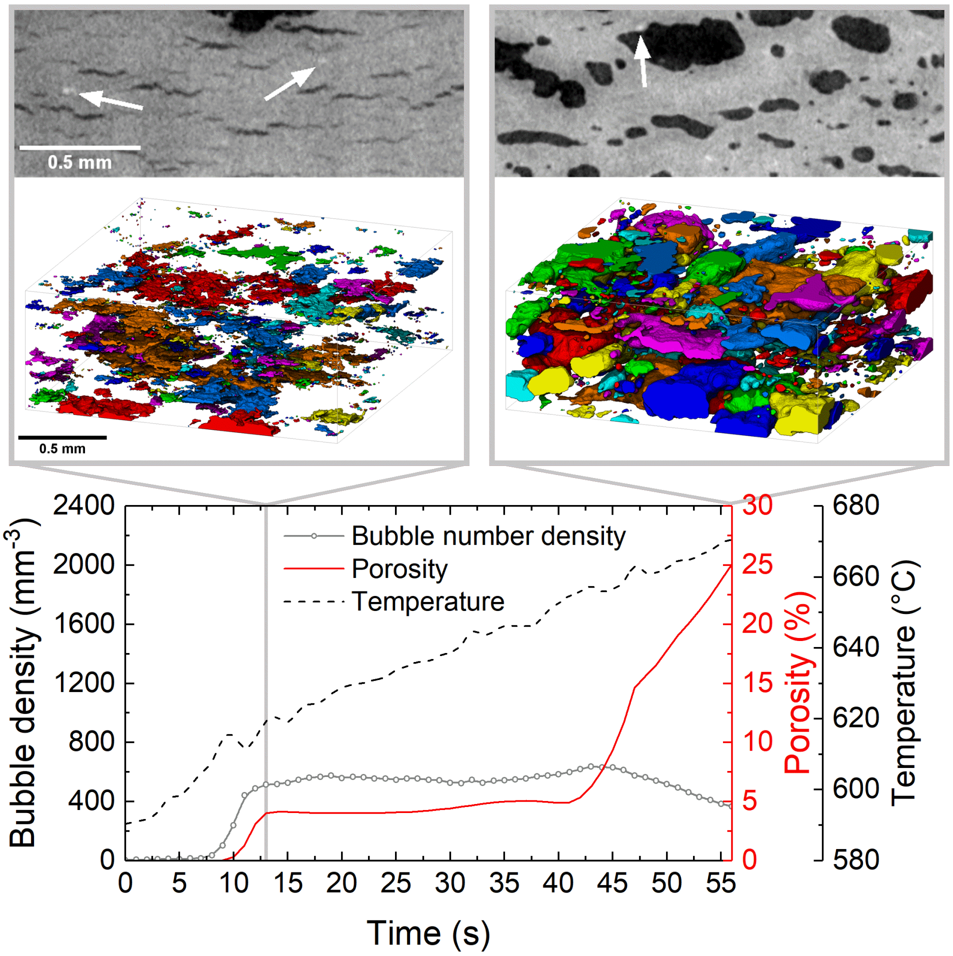

Fig. A.1: Early foaming stage (porosity <25 %) of pure Al. Vertical sections through the tomograms and 3D images of the separated bubbles (top) show the moment of the first porosity increase (left pictures, *t* = 13 s) and when the porosity reaches 25 % (right pictures, *t* = 56 s). The graph below shows the temperature curve as well as the bubble density and porosity over the experiment time.

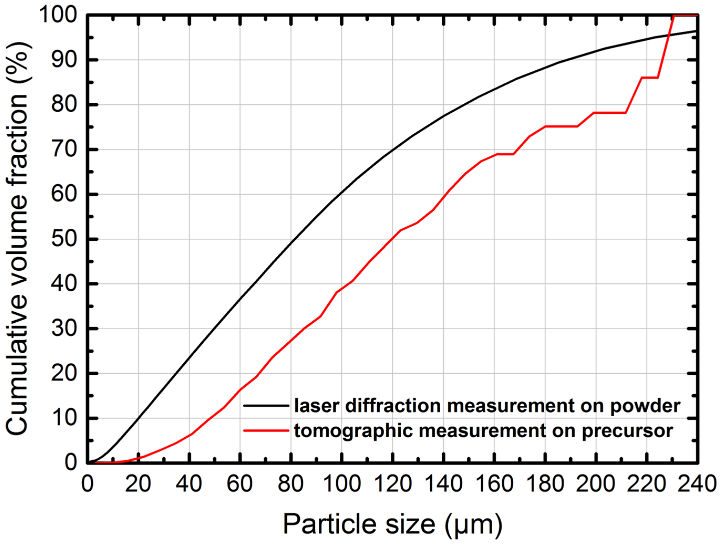

Fig. A.2: Cumulative volume fraction of AlMg50 particles measured by laser diffraction analysis on as received powders (black) and through tomographic imaging on the consolidated precursor (red).

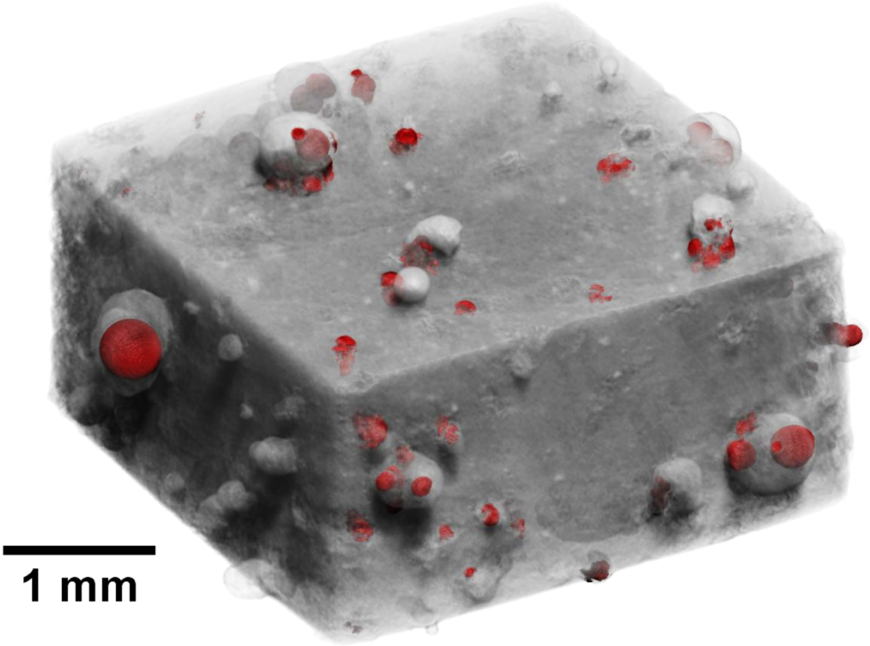

Fig. A.3: 3D rendering of a full field tomogram taken at the point of maximum melt ejection from a precursor with only large AlMg50 particles at 538 °C. Bubbles shown in red extend (within a melt droplet) from the sample surface

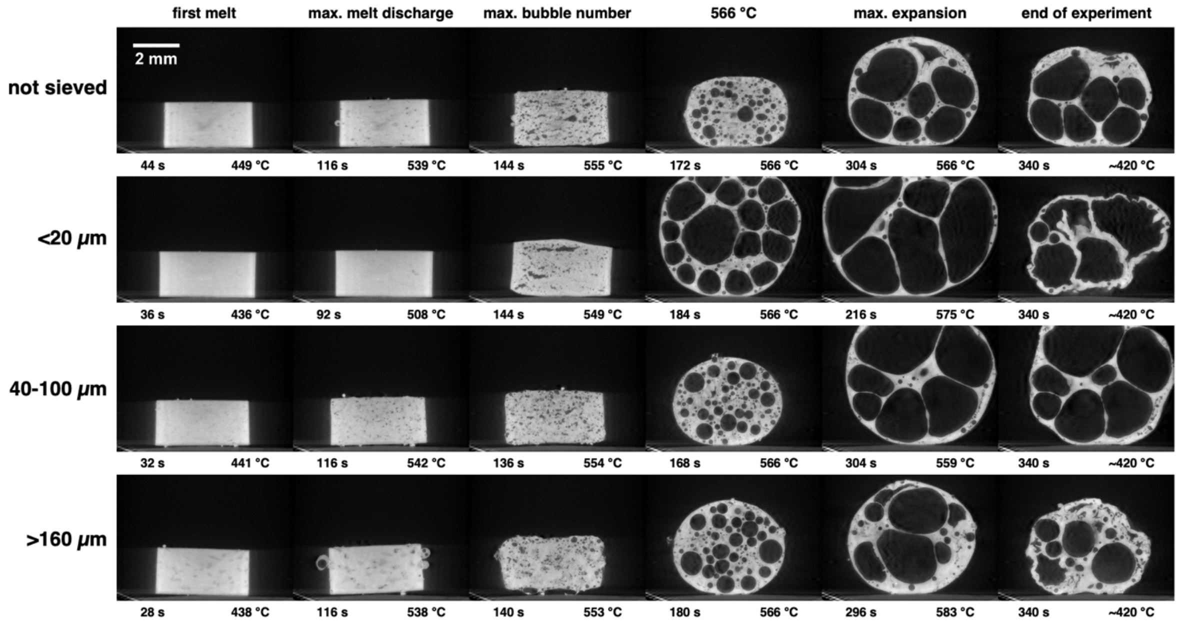

Fig. A.4: Vertical slices through tomograms at different stages of foaming of AlSi8Mg4 with 0.25 wt% TiH_2 and different AlMg50 powder particle size distributions (non-sieved, <20 µm, 40–100 µm and >160 µm) with the full sample inside the field of view. Heating was carried out with increasing laser power and a subsequent holding time of 180 s up to a temperature of about 580 °C at 295 s experiment time.

Table A.1: Comparison of bubble number and volumetric expansion of the samples from Fig. A.4 for the last four different stages of foaming.

Particle size	Number of bubbles (-) / Volume expansion (-)			
	max. bubble number	**566 °C**	**max. expansion**	**end expansion**
not sieved	22640 / 1.3	19026 / 1.6	11747 / 2.9	8685 / 2.7
<20 µm	14065 / 1.3	>7964 / >3.3	>5771 / >5.8	1775 / 3.4
40-100 µm	23011 / 1.3	14222 / 1.9	>7464 / >4.7	>5829 / >4.4
>160 µm	17967 / 1.3	8568 / 1.9	5761 / 2.8	4285 / 2.1

Supplementary material

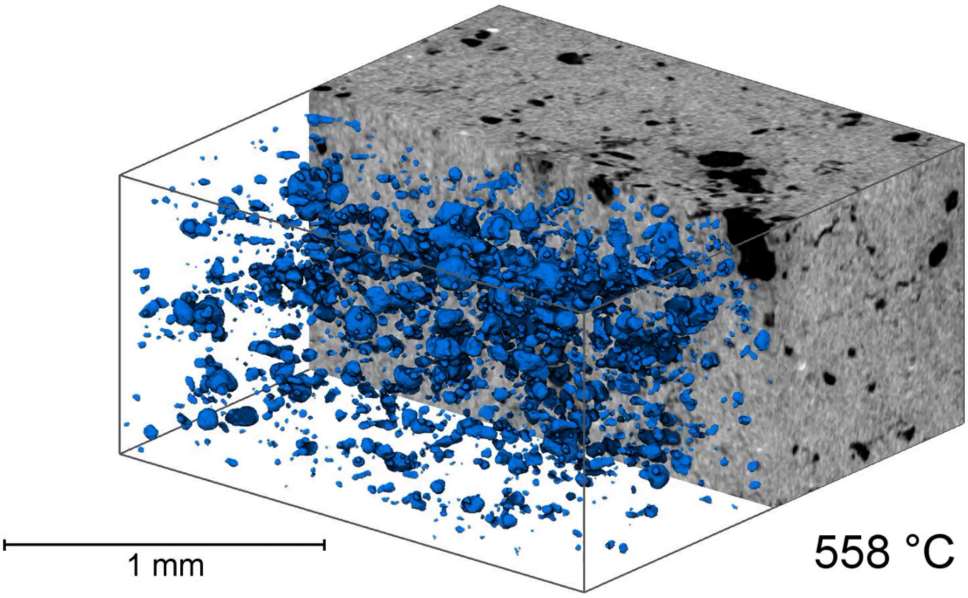

Video 1: Time-resolved 3D rendering of the developing bubbles (blue) during the transition from the first to the second nucleation stage in a cut-out volume of the foamable AlSi8Mg4 precursor (10x speed).

Link: tomoscopy.net/videos/nucleation/alsi8mg4_transition_10x.mp4

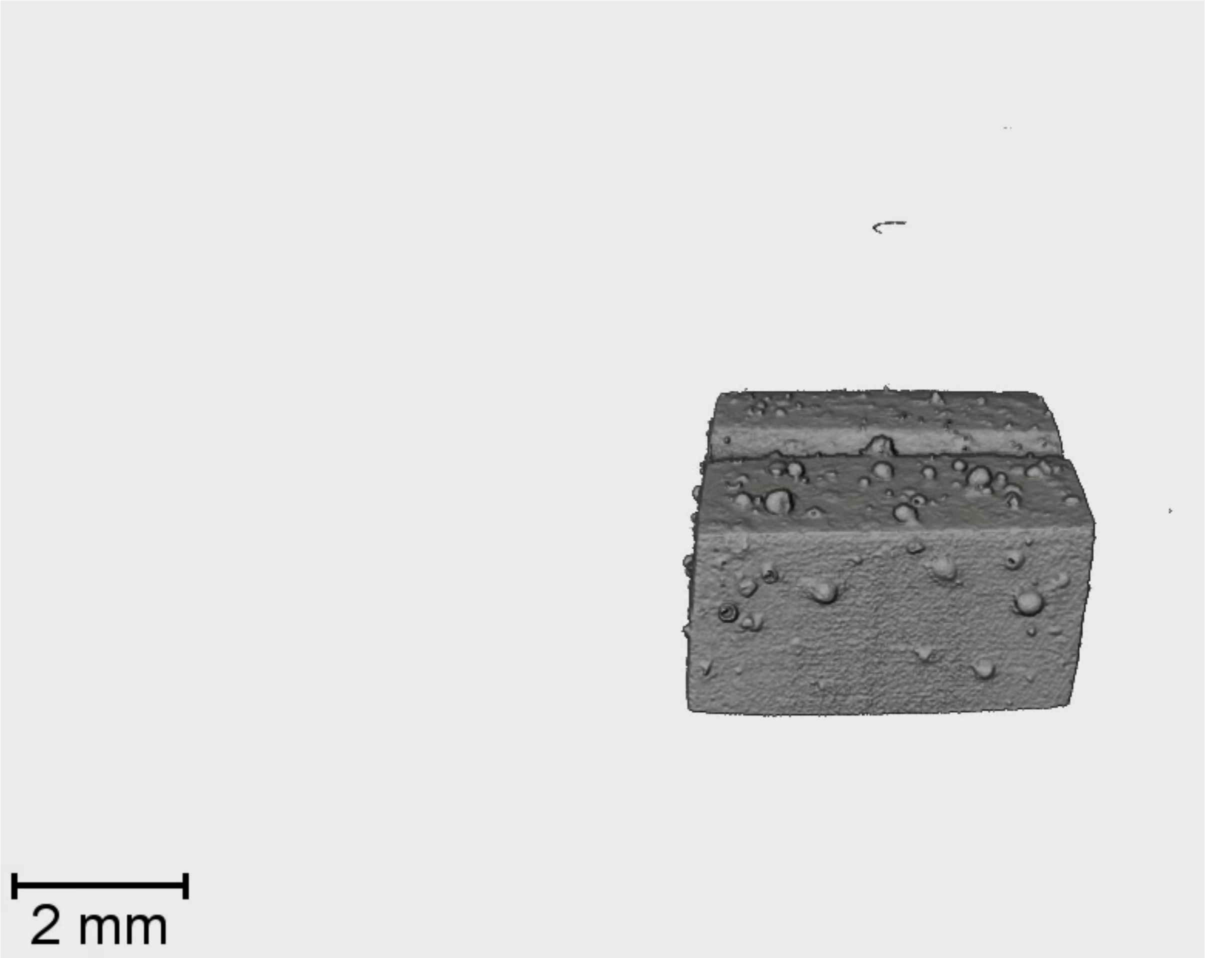

Video 2: Time-resolved 3D surface rendering of an evolving full field AlSi8Mg4 foam (10x speed).

Link: tomoscopy.net/videos/nucleation/melt_ejection_10x.mp4

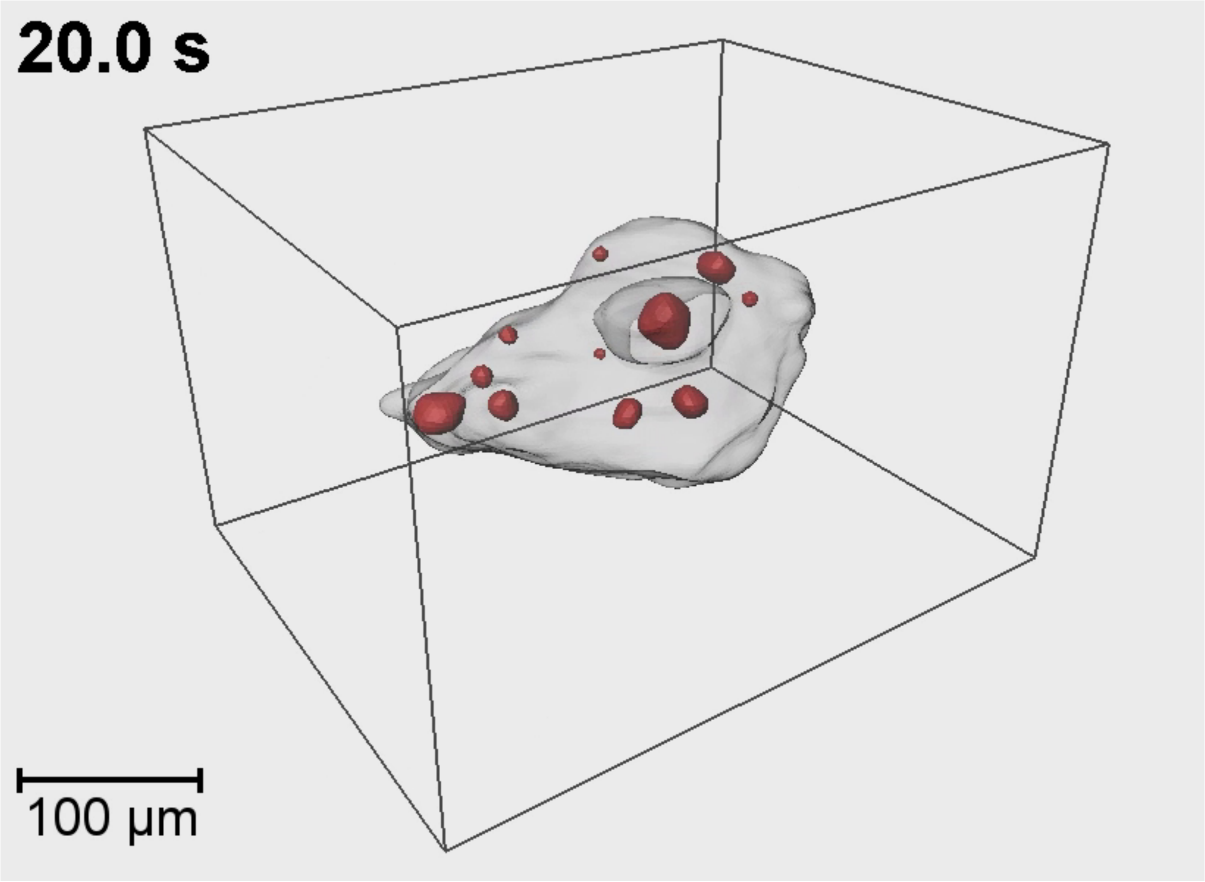

Video 3: Time-resolved 3D rendering of evolving bubbles (red) in one individual AlMg50 particle (2x speed).

Link: tomoscopy.net/videos/nucleation/bubbles_in_particle_2x.mp4